Mitigation of Nacelle/Pylon Wake on the High-Lift Common Research Model Using a Nacelle Chine

Mehti Koklu[*], John C. Lin[†], Judith A. Hannon[‡], Latunia P. Melton[§],
Marlyn Y. Andino[**], Keith B. Paschal[††], and Veer N. Vatsa[‡‡]

NASA Langley Research Center, Hampton, VA, 23681, USA

A 10% scale, high-lift version of the Common Research Model (CRM-HL) was tested in the NASA Langley Research Center 14- by 22-Foot Subsonic Tunnel. The focus of the wind tunnel test campaign was to assess the feasibility of active flow control (AFC) on the simplified CRM-HL configuration. The modular design of the CRM-HL model enabled the testing of the conventional CRM-HL version to establish a benchmark for the AFC research. The wind tunnel model has the capability of being tested with and without the engine nacelle/pylon for comparison. The wind tunnel investigation included the acquisition of force and moment data, steady pressure data, as well as surface flow visualization using minitufts. For some select cases, numerical simulations were performed to aid in understanding the wind tunnel data. Wind tunnel measurements indicated a lift degradation of the conventional CRM-HL at high angles of attack. The surface flow visualization with fluorescent minitufts revealed that the lift degradation is due to flow separation caused by the nacelle/pylon wake on the inboard wing. The wake and the consequent flow separation were successfully mitigated using a nacelle chine installed on the inboard side of the engine nacelle.

I. Nomenclature

α	=	angle of attack
C_D	=	drag coefficient
C_L	=	lift coefficient
C_{Lmax}	=	maximum lift coefficient
C_p	=	pressure coefficient
C_{Pt}	=	total pressure coefficient
λ_2	=	second eigenvalue of the velocity gradient tensor
U'_n	=	transverse fluctuating velocity
u', v', w'	=	standard deviation of velocities along the *x, y, z* coordinates, respectively
φ, ψ, θ	=	local flow direction angles between the *x, y, z* coordinates, respectively
x, y, z	=	longitudinal, lateral, and normal axes, respectively

II. Introduction

Within the framework of efficiency and environmental compatibility goals, the NASA Advanced Air Transport Technology (AATT) Project explores improved high-lift concepts that have less part counts, are less complex, are lighter, and more importantly provide drag reduction without sacrificing the aerodynamic performance during takeoff and landing operations. One viable option is to use simplified high-lift (SHL) systems with simple-hinged flaps [1]. The simple-hinged flaps are the simplest and the most basic flaps for high-lift systems; however, they are vulnerable

---

[*] Research Scientist, Flow Physics and Control Branch, MS 170
[†] Senior Research Scientist, Flow Physics and Control Branch, MS 170, AIAA Associate Fellow
[‡] Research Scientist, Flow Physics and Control Branch, MS 170
[§] Senior Research Scientist, Flow Physics and Control Branch, MS 170, AIAA Associate Fellow
[**] Research Scientist, Flow Physics and Control Branch, MS 170, AIAA Senior Member
[††] Research Scientist, Flow Physics and Control Branch, MS 170
[‡‡] Senior Research Scientist, Computation AeroSciences Branch, MS 128, AIAA Associate Fellow

to flow separation that is detrimental to the aerodynamic performance during takeoff and landing operations [1-4]. The SHL systems are capable of attaining the required aerodynamic performance only if the flow separation over the flap is controlled, for example, using an Active Flow Control (AFC) system.

In order to demonstrate the feasibility of the AFC-enabled SHL systems, a 10%-scale, high-lift version of the Common Research Model (CRM-HL) was built. The CRM-HL geometry is open to the public and intended to be used in R&D efforts related to aerodynamic efficiency, noise reduction, high-lift aerodynamics/flow physics, and CFD development/validation [5]. The semispan CRM-HL model is representative of a modern civil transport aircraft and includes both the conventional and AFC-enabled SHL systems. As a relevant high-lift geometry, the CRM-HL model can serve as a high-lift technology development platform and the performance levels achieved by the geometry can be a reference for the conventional high-lift systems [6]. Although the focus of the wind tunnel test was to assess the feasibility of active flow control (AFC) on the simplified CRM-HL configuration [5, 7-8], the wind tunnel test matrix also included the conventional CRM-HL version to establish a benchmark for the AFC research. The conventional CRM-HL model features a three-element high-lift configuration that includes a slat, a main wing, and a single slotted Fowler flap [5-6]. In addition to the main three elements, the relevant commercial transport geometry involves many parts such as fuselage, nacelle, pylon, chine, leading edge strake, flap fairings, and slat brackets. Flow over multielement airfoils is complex in nature (see Refs. 9-10 for more details about the high-lift aerodynamics) and inclusion of the flow interactions with these parts in a relevant geometry makes it even more complex. A.M.O. Smith [9] provided a theoretical basis for high-lift aerodynamics and insight into the underlying aerodynamic principles. The integration of an engine nacelle to the airframe produces many discontinuous surfaces and the resulting flow physics is dominated by a variety of interacting flow phenomena, such as wakes, discrete vortices, laminar and turbulent boundary layers, and unsteady separated flow [11].

Along with the advancement in the aircraft industries in general, the aircraft jet engines are constantly improving and resulting in larger diameter engines. The integration of the large-diameter nacelles is challenging and negates some of the aerodynamic efficiency improvements. This is because a wing-mounted engine nacelle usually requires a structural strut (i.e., pylon), which, together with the engine nacelle, reduces the maximum lift, C_{Lmax}. C_{Lmax} is a critical parameter for sizing high-lift systems and hence for the overall aircraft wing size and performance [10]. Although this penalty is alleviated by leading-edge slats [10], a large-diameter nacelle requires a cutout of the slat to install the nacelle and pylon on the airframe. The cutout in the slat also has its own associated penalties. The obvious one is the interruption of continuous slat deflection. The other penalty of the slat cutout is the contamination of the downstream flow field by the wake/vortices generated at the cutout corners resulting in a flow that is very sensitive to flow separation (i.e., nacelle wake separation). An ingenious way of alleviating some of the adverse effects of the nacelle/pylon/slat/slat cutout interference is to use a nacelle chine. The nacelle chine, sometimes referred to as a nacelle strake, is basically a vortex generator that produces a strong streamwise vortex that travels along the upper surface of the wing. This streamwise vortex interacts with the nacelle/pylon wake and recovers the maximum lift performance of the aircraft.

After the discovery of nacelle chines during the 1970s, they were quickly adopted by aircraft manufactures and commonly used on airliners. Although the first implementation was to use a pair of chines on the nacelle [12] of the DC-10 planes [13], the outboard chine has been omitted in the current usage. The nacelle/pylon wake and its control with a nacelle chine has been the subject of many studies. For example, as part of the EUROLIFT project, a complete high lift system, including pylon, nacelle, and nacelle chine of a realistic commercial-type aircraft configuration, was investigated experimentally [14]. The nacelle/pylon wake and its control were also studied numerically in Refs. 15 - 17. AFC actuators, such as steady/pulsed blowing [16] and fluidic oscillators [17], were also implemented to alleviate the adverse effects of the nacelle/pylon wake. Another wind tunnel test campaign was conducted by JAXA, where a realistic high-lift configuration, JSM, (JAXA Standard High Lift Model), was used to investigate the nacelle/pylon wake and its control with a nacelle chine [18]. The installation of the nacelle chine was explored and optimized using an efficient global optimization technique [19]. The JSM configuration was selected as a test case for the AIAA High-Lift Prediction Workshop and many computational results have been provided by workshop participants [20].

The main objective of this research is to investigate the wake and its subsequent flow separation generated at the nacelle/pylon/wing region of the CRM-HL configuration. The mitigation of this wake and the associated flow separation using a nacelle chine is another objective of this study. Numerical simulations are used in addition to the wind tunnel measurements to investigate this complex flow field.

III. Experimental Setup

The experimental setup including the wind tunnel, model, and the test conditions was reported elsewhere [21, 5-6]; therefore, only a summary will be given for completeness. The wind tunnel test was conducted in the NASA Langley

Research Center 14- by 22-Foot Subsonic Tunnel (14x22). The 14x22 is an atmospheric, closed return wind tunnel with a 14.5-ft high, 21.8-ft wide, and 50-ft long test section [21]. The wind tunnel tests were performed at a nominal freestream Mach number of 0.2 and a corresponding Reynolds number based on the mean aerodynamic chord of approximately of 3.27×10^6. For this wind tunnel entry, no boundary layer trips were applied to the model surface to allow for natural transition. The experimental measurements included forces and moments, surface static pressures, surface unsteady pressures, model deformation, and surface flow visualization. Surface flow visualizations were performed using fluorescent minitufts, which were fabricated using general purpose thin sewing thread. The tufts were prepared on a tape strip and then applied on the model surface. In tuft flow visualization images, the motion blur indicates unsteady flow and direction reversal indicates flow separation. The details about tuft flow visualization can be found in Ref. 22.

The model tested in this study is the 10%-scale, high-lift version of the NASA Common Research Model [23]. A photo of the CRM-HL in the 14x22 wind tunnel and its CAD drawing are shown in Fig. 1. The details of the CRM-HL model can be found in the papers by Lin et al. [5] and Lacy et al. [6]. A simplified version of the CRM-HL model (without nacelle/pylon, brackets, fairings, and leading-edge strake) was selected as one of the test cases for the AIAA High-Lift Prediction Workshop and is currently available on the workshop website [20]. The 9.6 ft. high semispan model was installed vertically on the turntable on the tunnel floor (Figs. 1-2). The length of the fuselage is 20.6 ft. The slat and the flap deflection angles were 30° and 37°, respectively, and remained the same throughout the test. In this wind tunnel entry, the horizontal tail was not installed. The CRM-HL model includes a flow-through fan cowl that is attached to the wing with a pylon. Design of the nacelle and pylon is similar to that of the high-speed CRM [23] with a few modifications described in Ref. 6. Key components of the CRM-HL model (such as flaps, slats, nacelle/pylon, and horizontal tail) are all modular and reconfigurable. The modular design enabled the model to be switched between different configurations while keeping the other components the same. The pressure data presented in this paper do not include the wind tunnel wall corrections to facilitate a direct comparison with the numerical simulations. There are approximately 900 pressure taps mostly populated in streamwise arrays at eight spanwise stations. The locations of the static pressure taps on the model are depicted by dots in Fig. 2. Note that the position of the pressure taps in the streamwise (x) direction is based on the deflected configuration, whereas, they are based on the stowed configuration in the spanwise (y) direction. This is because coordinates for the deflected slats and flaps are not in alignment with the freestream direction. The model includes 15 slat brackets and three flap brackets. The slat brackets were designed with channels for routing the pressure tubing to the wing under slat surface (WUSS), hence eliminating the need for routing the tubing bundles external to the brackets. The flap brackets were covered by polycarbonate flap fairings.

Numerical simulations were also performed in order to complement the wind tunnel data. A commercial software package based on the Lattice Boltzmann Method (LBM) [24] was used to simulate the three-dimensional (3D), compressible, unsteady flow over the CRM-HL model. A modified k−ϵ turbulence model, which involves a very large eddy simulation approach, was used to resolve the large energy containing scales. In addition, appropriate wall functions [25] were utilized to capture the boundary layer behavior without excessive grid resolution near the solid walls. The LBM equations were solved on embedded Cartesian meshes (voxels), which were successively refined near the high-gradient regions using variable resolutions. The numerical model used an explicit time advancement scheme that allowed massively parallel simulations. The computational modeling included the same details of the 3D CRM-HL geometry, comprised of the main wing, fuselage, nacelle, pylon, slat, flap, leading edge strake, flap fairings, and slat brackets. Computational Fluid Dynamic (CFD) simulations were performed for the in-tunnel mode (with tunnel walls) similar to the experiment. The details of the computational setup and the simulation method can be found in Ref. 26.

Although the CFD simulations provided a wealth of information, they are used herein to better understand the qualitative flow characteristics but not necessarily for CFD code validation purposes. The quantitative comparison of the numerical results with the experimental data will be the subject of another study. In the numerical results, we focused on the surface flow characteristics and the off-surface total pressure contours to study the flow structures that developed on the model. The surface streamlines were superpositioned on the near-surface transverse-fluctuating velocity, U'_n, which is a function of the standard deviations of the velocities. The motivation behind using this term is to represent the flow unsteadiness observed by the tufts. Since the model, and hence the flow, is three dimensional, the transverse fluctuating velocity is not necessarily the fluctuating velocity in the spanwise direction; rather, it is the fluctuating component that is normal, or transverse, to the local flow direction. For a 3D flow, the transverse fluctuating velocity is:

$$U'_n = u'|\sin(\varphi)| + v'|\sin(\psi)| + w'|\sin(\theta)|$$

where u', v', w' are the fluctuating velocities and φ, ψ, θ are the local flow angles in x, y, z directions, respectively.

IV. Results

The main focus of this study is the investigation of the nacelle/pylon wake, its associated flow separation, and control of the flow separation using a nacelle chine. In all the results, the freestream Mach number was 0.2. The slat and flap deflection angles were 30° and 37°, respectively. No slat/flap rigging study was performed in this wind tunnel entry, and the nominal values for the landing configuration presented in Ref. 5 were used. Note that the wind tunnel measurements presented in this study were acquired while the tufts were present on the model. Although the tufts could alter the wind tunnel measurements depending on the tuft material and how they are applied [27], it was shown previously that the fluorescent minitufts used in this test have negligible effect on the wind tunnel measurements [22]. The nonintrusiveness of the minituft technique was also reported in a range of low and high-speed wind tunnel tests [28].

The results section is divided into four subsections. In the first subsection, the baseline configuration over the CRM-HL model will be discussed. The baseline configuration is referred to as the case where the nacelle/pylon is installed without any nacelle chine. Although the wind tunnel measurements covered the entire angle of attack range (from $\alpha = -4°$ to $\alpha = 19°$), select angle of attack cases, $\alpha = 8°$, 12°, 16°, and 18°, are presented for brevity. Since the wake of the nacelle/pylon is more dominant over the inboard wing at higher angles of attack, the results are focused mainly on the inboard wing at near stall ($\alpha = 16°$) and at poststall ($\alpha = 18°$) conditions. In the second subsection, the discussion will be focused on the model configuration where the nacelle/pylon was removed. With the absence of the nacelle/pylon and its consequent wake, this is a target case for flow separation control. In other words, the metric for the effectiveness of a given chine can be determined by how well it helps recover the aerodynamic performance of a clean wing. In the third section, results obtained with a nacelle chine installed on the inboard side of the nacelle will be discussed. The location of the nacelle chine was refined to find the best case. In the last section, numerical simulations are presented and discussed for the baseline and flow control cases at the near stall and poststall conditions.

A. Baseline Configuration

The baseline configuration is a complete high-lift configuration including a nacelle and a pylon without any flow control (i.e., no chine). Aerodynamic performance of the CRM-HL model is presented in Fig. 3. As shown in the lift curve (Fig. 3a), the lift values deviate from the constant-slope trend at higher angles of attack indicating an aerodynamic performance loss before maximum lift is achieved. As will be shown later, this lift loss is due to flow separation on the inboard wing that is caused by the nacelle/pylon wake. Mitigation of this wake and its associated flow separation are the subject of this study. Since the drag coefficient has a linear relationship with C_L^2 in theory [27], the induced drag characteristics (C_D vs. C_L^2 plot) in Fig. 3b also point out the performance degradation for higher angles of attack. The drag values deviate from the linear relationship for $\alpha > 12°$ and generate higher than expected drag for the same lift.

Streamwise pressure distributions at select spanwise sections give insight into the overall flow topology at different angles of attack. Figures 4-6 show C_p distributions on the inboard ($y = 27.8$ in), midboard ($y = 63.8$ in.), and outboard ($y = 94.7$ in.) sections, respectively. The locations of these streamwise arrays on the CRM-HL model were displayed in Fig. 2. As expected, we see higher suction pressures on the slat and on the main wing as the angle of attack increases, whereas, the near stall ($\alpha = 16°$) and poststall ($\alpha = 18°$) angles provided similar pressure distributions. This statement is valid for the inboard, midboard, and outboard sections. On the other hand, the suction pressures on the inboard flap for the near stall and poststall conditions are significantly reduced. At lower angles of attack ($\alpha = 8°$ and $\alpha = 12°$), the inboard flap exhibits a complete pressure recovery. Increasing α further results in lower suction pressures on the inboard flap and possibly flow separation for $\alpha > 12°$ (see inset figure in Fig. 4). On the outboard flap, the C_p distributions are not significantly affected by α and are comparable (Fig. 5). The pressure distributions on the outboard flap indicates flow separation near the flap trailing edge.

Figures 7a and 7b show the spanwise C_p distributions near the leading edge and midchord of the main wing, respectively. The background image shows the location of the spanwise pressure taps as well as the engine nacelle to help interpret the pressure distributions. As expected, the suction pressures on the main wing increase with α. The effect of the engine nacelle is noticeable especially in the upstream spanwise C_p distributions. The dip in the C_p distributions near $y = 38$ in. corresponds to the slat cutout where there is no slat due to the pylon/airframe integration. The reduction in the suction pressure is caused by the wake generated by the nacelle/pylon. The spanwise C_p distributions along the midchord appear to be skewed toward the outboard side of the wing (Fig. 7b). We see gradual increases in the suction pressures on the outboard side as α increases. The poststall ($\alpha = 18°$) condition produces a similar C_p distribution to that of the near stall ($\alpha = 16°$) condition on the outboard side. On the inboard side, the suction pressures increase until $\alpha = 12°$. For $\alpha > 12°$, the suction pressures drop slightly for the near stall ($\alpha = 16°$) condition

as the effect of nacelle/pylon wake increases and drop substantially for the poststall ($\alpha = 18°$) condition when the wake becomes disruptive.

Figure 8 shows the tuft flow visualization at $\alpha = 8°$ that focused on the inboard wing. All flow visualization images show the upper surface of the model, where the freestream flow is from left to right. The flow over the main wing, fuselage, and nacelle appears fully attached. As depicted on the figure, the tufts indicate flow unsteadiness downstream of the nacelle/pylon that is possibly due to the wake generated by the nacelle/pylon. At this angle of attack, this flow unsteadiness is weak and decreases downstream. The flow over most of the inboard flap is attached except for a flow separation bubble between the flap and fuselage, and the local separated flow upstream of the flap fairing. This local separated flow is possibly caused by the obstruction of the flap slot by the fairings on the lower side of the wing. Therefore, in addition to causing parasitic drag during cruise conditions, the flap fairings act as a constriction to the flow from the flap slot resulting in flow separation and hence performance losses during high-lift operations. Increasing the angle of attack further ($\alpha = 12°$) resulted in some minor changes in the surface flow topology (Fig. 9). The $\alpha = 12°$ case is important because the slope of the lift curve in Fig. 3a starts to change near $\alpha = 12°$. Note that the background image that shows the model features was removed to increase the contrast in the tuft visualization images. As indicated by the unsteady tufts, the unsteady flow region becomes larger. This is because, at this angle of attack, the stagnation point moves downstream on the lower surface of the wing (not shown here) and the nacelle/pylon generates a stronger wake. There is no noticeable difference in the surface flow over the main wing, fuselage, and nacelle, as it remains attached. Flow over most of the inboard flap appears to be attached as well.

The tuft flow visualization at the near stall condition ($\alpha = 16°$) is presented in Fig 10. Most of the flow remains attached; however, the tuft flow visualization indicates flow separation near the main wing trailing edge as depicted on the figure. The tufts on the inboard flap demonstrate unsteady flow and possibly flow separation near the trailing edge. This is consistent with the C_p distributions given in Fig. 4, which showed a substantial drop in the suction pressures on the inboard flap compared to the lower α cases. These separated flow regions are the reason for the lift performance degradation (Fig. 3). At the poststall condition ($\alpha = 18°$), the developing flow structures at lower α have become disruptive for the inboard region (Fig. 11). The nacelle/pylon wake dominates most of the inboard wing. Flow separation, triggered by the nacelle/pylon wake, extends to the leading edge of the main wing. The extended flow separation is in line with the pressure anomaly in the spanwise C_p distribution for the $\alpha = 18°$ case (near $y = 30$ in. Fig. 7b). A wing-body separation bubble appears near the main wing trailing edge that affects both the main wing and the fuselage (Fig. 11). The flow separation causes substantial suction-pressure reduction near the fuselage ($y = 12.3$ in. in Fig. 7b) in the spanwise C_p distributions. Flow visualization on the inboard flap region indicates flow patterns similar to those of the $\alpha = 16°$ case, which is also consistent with C_p distributions in Fig. 4. Different from the near stall condition, the tuft flow visualization indicates separated flow over the nacelle upper surface at the poststall condition ($\alpha = 18°$).

A representative tuft flow visualization on the outboard wing is presented in Fig. 12 for a low ($\alpha = 8°$) and a high ($\alpha = 16°$) angle of attack. It was shown previously [22] that the flow on the outboard wing does not change significantly with angle of attack. The outboard wing exhibits attached flow except for the outboard flap, where the flow has a strong spanwise component due to the change in the flap sweep angle. The flow between the two outboard flap fairings is dominated by unsteady spanwise flow. Tuft flow visualization indicates 3D flow separation on the outboard flap (notice the first tuft array points downstream; whereas, the last tuft array points slightly upstream) that appears similar for the low ($\alpha = 8°$) and high ($\alpha = 16°$) angles of attack. The difference between the low and high angles of attack can be observed on the aileron section where the higher angle of attack cases exhibit pockets of local flow separation regions downstream of the slat brackets near the trailing edge (Fig. 12b). These pockets of local flow separation are caused by the interaction of the slat bracket wakes with the APG and are not present for low angles of attack (Fig. 12a). The separated flow due to the slat bracket wake was also shown in the numerical simulations [22].

B. No Nacelle Pylon Configuration

It was shown in the previous section that the aerodynamic performance degradation at higher angles of attack is due to the flow separation caused by the nacelle/pylon wake. In order to isolate the effect of this wake on the aerodynamic performance, the nacelle pylon (i.e., the source of the wake), was removed and the model was tested at the same experimental conditions. A picture of the CRM-HL model without the nacelle/pylon in the 14x22 tunnel is given in Fig. 13. Note that the model is designed to have a continuous slat and a continuous WUSS in the spanwise direction when the nacelle/pylon is removed.

The aerodynamic performance of the CRM-HL model without the nacelle/pylon is presented in Fig. 14. The no nacelle pylon (NNP) case produces a lift coefficient that is similar to the baseline case in the linear range $\alpha < 12°$. After this point, while the NNP case has a near-constant slope until C_{Lmax}, the baseline case shows lift degradation resulting in a drop in the lift coefficient as much as $\Delta C_L = 0.1$ (Fig. 14a). Figure 14b shows that the induced drag also

has a linear relationship until C_{Lmax} for the NNP case but the induced drag of the baseline case deviates from the linear relationship for the higher angles of attack producing larger than expected drag values. Although the elimination of the flow separation over the inboard wing also contributes, the main reason for the substantial drag reduction is the elimination of the nacelle/pylon itself (i.e., less profile drag). In addition to the lift degradation, the induced drag characteristics highlight two distinct features (Fig. 14b). First, the curve is shifted to the right clearly showing the NNP case produces lower drag. Second, the slope of the curve for the NNP case is slightly smaller than that of the baseline case indicating that the drag of the nacelle increases with angle of attack. This is because the nacelle is less aligned with the flow at higher angles of attack and its blockage (or area) increases, thus, increasing drag.

Figure 15a compares the C_p distribution on the inboard wing ($y = 27.8$ in.) to that of the baseline case for the near stall condition (at $\alpha = 16°$). The NNP case provided considerably higher suction pressures on the entire wing with the exception of the slat, where the suction peak appears to be lower than that of the baseline case. The effect of the nacelle/pylon and its generated wake is more pronounced over the flap. In the absence of the nacelle/pylon wake, the flow over the flap produces higher suction pressures and provides a better pressure recovery compared to the baseline case. At this location, the flow appears to be attached for the NNP case; whereas, it is separated for the baseline case. Figure 15b compares C_p distributions of the NNP and the baseline cases near the midspan of the model ($y = 63.8$ in.). Since this location is outside the nacelle/pylon wake, both cases produced similar pressure distributions as expected.

The spanwise C_p distributions near the leading edge and midchord of the main wing are presented in Fig.16. The effect of the nacelle manifests as a dip in the pressure distributions downstream of the nacelle in the baseline case. This dip does not exist in the NNP case. Outboard of the midspan, both C_p distributions have similar trends with the NNP case producing slightly higher suction pressures. The spanwise C_p distributions along the midchord of the main wing also demonstrate the effect of the nacelle/pylon wake. There is an offset in the pressure levels over the inboard wing, where the nacelle/pylon wake is dominant. This effect decreases gradually in the spanwise direction (i.e., moving away from the wake) and both configurations produce similar pressure levels outboard of the midspan.

Figure 17 displays the streamwise C_p distribution of the NNP case at the near stall ($\alpha = 16°$) and poststall ($\alpha = 18°$) conditions on the inboard wing ($y = 27.8$ in.) where the effect of the nacelle/pylon wake normally would be seen. The C_p distributions indicate pressure recovery without any flow separation (see flap trailing edge). Due to the increased adverse pressure gradient, the $\alpha = 18°$ case produced lower suction pressures over the flap and near the main wing trailing edge. This is compensated by the higher suction pressures over the slat and near the main wing leading edge providing comparable lift values for the near stall and poststall conditions (see Fig. 14a). Consistent with the C_p distributions, the tuft flow visualization images do not indicate any noticeable difference between the near stall ($\alpha = 16°$) and poststall ($\alpha = 18°$) conditions (Fig. 18). In the absence of the nacelle/pylon and its associated wake, the flow over the inboard wing is attached for both angles of attack. The tufts on the main wing and on the flap appear to be streamlined without any sign of flow separation even for the poststall condition, where the baseline case showed severe flow separation that covered most of the inboard wing (see Fig. 11).

C. Flow Separation Control with the Nacelle Chine
As clearly shown in the previous sections, the nacelle/pylon generates a wake that interacts with the adverse pressure gradient (APG) and causes flow separation at higher angles of attack ($\alpha > 12°$). Flow separation dominates the flow over the inboard main wing and moves upstream as the angle of attack increases. In addition, the wake and the separated flow also interact with the flow from the inboard flap slot, which results in lower suction pressures and possibly flow separation on the flap. These adverse effects of the nacelle/pylon wake and the associated flow separation manifest themselves as a lift performance degradation. The NNP case confirmed that the lift performance loss is due to the nacelle and it is as much as $\Delta C_L = 0.1$. Although there are active flow control methods proposed in the literature [16-17], the simplest way of controlling flow separation is using a nacelle chine. The nacelle chine, sometimes called a nacelle strake, is basically a vortex generator. The strong streamwise vortex generated by the nacelle chine improves the flow over the wing by reducing the nacelle/pylon wake and mitigating flow separation. The picture of the nacelle chine used in this study is given in Fig. 19. The nacelle chine is a 6.2 in. long, 1.86 in. high, gothic type vortex generator. The apex of the nacelle chine is located approximately 7 in. downstream of the nacelle leading edge and is skewed approximately 6° to the incoming flow on the inboard side of the nacelle. The location of the nacelle chine is shown in the zoomed-in image Fig. 19b.

One of the important parameters for the nacelle-chine application is the location of the chine. In this study, three-different chine locations were investigated. The streamwise location of the nacelle chine was fixed (see Fig. 19b) but the circumferential position was varied. The circumferential position is defined as the azimuthal angle starting from the pylon (i.e., from the normal axis) in the clockwise direction when looking downstream at the front of the nacelle. In the first configuration (Chine#1), the apex of the nacelle chine was placed an approximate azimuthal angle of 34°. The resulting lift coefficient is compared to that of the baseline case in Fig. 20a. Since the nacelle/pylon wake is

dominant at higher angles of attack, the figure is zoomed into the C_{Lmax} region. As expected, there is no significant effect at lower α ($\alpha < 12°$) as the nacelle/pylon wake is less pronounced. Application of the nacelle chine greatly improves the lift performance, increases the C_L as much as 0.08, and extends the linear range to 14°. The stall angle appears not to be affected by the nacelle-chine. In the second configuration (Chine#2), the nacelle chine was moved to an approximate azimuthal angle of 39°. As shown in Fig. 20a, the lift performance is enhanced slightly, especially between $14° < \alpha < 16.5°$. The improvement is limited and shown as an increase in the slope. In the last configuration (Chine#3), the nacelle chine was moved to an approximate azimuthal angle of 45°. At this location, the lift performance is further improved. The resulting lift curve is smooth without any apparent performance degradation (Fig. 20a). This case was used as a reference for the AFC version of the CRM-HL model.

Figure 20b demonstrates the effect of the nacelle chine on the drag coefficient. In order to see the effect on the drag independent of the lift, the drag coefficient was plotted with respect to α in this first plot. Adding a nacelle chine increases the drag coefficient of the CRM-HL model. At lower α, the drag caused by a single nacelle chine is negligible. The drag increase is more pronounced at higher angles of attack ($\alpha > 12°$) where the lift performance is recovered. Comparing Figs. 20a and 20b, the drag increase at the same angle of attack is directly proportional to the lift increase; therefore, it is an outcome of flow separation control (i.e., lift induced drag). Since both the lift and drag increase with the chine application, the induced drag characteristics show the relative increments. As shown in Fig. 21, the increase in the lift coefficient is much greater than that of the drag coefficient due to the chine application. Indeed, the drag is shown to reduce for the same lift when the flow separation is controlled by a nacelle chine.

Representative C_p distributions for different chine configurations are presented in Fig. 22 for the near stall condition ($\alpha = 16°$) on the inboard wing ($y = 27.8$ in.) where the wake of nacelle/pylon is pronounced. The suction pressures on the slat and near the leading edge of the main wing are shown to increase slightly with the application of the nacelle chine. Therefore, the nacelle chine not only eliminates the flow separation on the main wing but also indirectly affects the upstream (i.e., slat) and downstream (i.e., flap) flow. On the other hand, since flow separation is eliminated, the flow over the main wing decelerates at a slower rate compared to the baseline case as shown by the higher suction pressures. The higher momentum flow is able to withstand the adverse pressure gradient, resulting in higher suction pressures and better pressure recovery on the flap. The pressure distribution on the flap also indicates the elimination of flow separation there as well. The Chine#1 configuration provides similar pressure recovery to the baseline case. The pressure recovery is improved slightly for the Chine#2 configuration; however, the Chine#3 configuration provides a complete pressure recovery with attached flow over the flap (see inset figure that shows the C_p distribution over the flap).

The nacelle chine provides marginal lift recovery at $\alpha = 18°$ (Fig. 23), and produces a negligible effect on downstream flow. This is also consistent with the lift curve (Fig. 20a) where all three chine configurations provide comparable lift performance for the poststall condition ($\alpha = 18°$). The spanwise C_p distributions also demonstrate the performance improvement with the nacelle chine application (Fig. 24). All three chine configurations significantly reduce the pressure loss downstream of the nacelle compared to the baseline case. This local improvement resulted in higher suction pressures throughout the span at this particular streamwise location. As shown, the midchord C_p distributions are also improved on the inboard wing where the nacelle/pylon wake is pronounced.

Figures 25 and 26 show the surface flow visualization of the three chine configurations along with the baseline case (Fig. 25a) for the near stall condition at $\alpha = 16°$. Since the effect of the nacelle chine is seen on the inboard wing, the tuft flow visualization images are zoomed into the main wing trailing edge and the inboard flap. As shown in Fig. 25b, the Chine#1 configuration eliminated the flow separation that existed in the baseline case. At the location where the baseline flow separated, we see wake-induced unsteadiness in the tufts. The unsteady flow interacts with the flow from the flap slot and creates local flow separation on the inboard flap. As a side note, particular attention should be paid to the effect of the slot and the slot jet. As explained by A.M.O Smith [9], the slot jet should not be considered as a type of wall jet that controls (i.e., energizes) the boundary layer. Unquestionably, the fresh boundary layer from the slot is thinner, withstands stronger pressure gradients, and is less likely to separate but should not be viewed as an active wall jet. A.M.O Smith called it one of the most common misconception of the slot effect and laid out five primary effects of the slots: slat effect, circulation effect, dumping effect, off-surface pressure recovery, and fresh boundary-layer effect. For more details about the effects of slots see Ref. 9.

Compared to the baseline case, where most of flow on the inboard flap is separated, the Chine#1 configuration reduced the inboard flow separation significantly and has only local regions of flow separation on the flap as depicted in Fig. 25b. This is consistent with the C_p distribution in Fig. 22 where the flap trailing edge pressures also indicated flow separation. The Chine#2 configuration does not create much difference in the surface flow patterns (Fig. 26a). The flow over the main wing remains attached with unsteady flow near the trailing edge, and possible local flow separation on the inboard flap. This also correlates with the lift values in Fig. 20a where the Chine#2 configuration increased the lift coefficient slightly. The pressure recovery on the flap is similar to that of the Chine#1 configuration

and indicates flow separation near the flap trailing edge (see inset Fig. 22). Surface flow visualization with Chine#3 is presented in Fig. 26b. The flow over the main wing remains attached and there is still unsteady flow (i.e., wake) as shown by the unsteady tufts. One of the major improvements with the Chine#3 configuration occurs over the flap where the local flow separation, seen in the baseline case, is eliminated and most of the flow over the inboard flap remains attached. This correlates with the flap C_p distributions (Fig. 22) where only the Chine#3 configuration indicated attached flow.

The aerodynamic performance of the CRM-HL model for the baseline, chine, and NNP cases are given in Fig. 27 and can be viewed as a summary of this study. Since the Chine#3 configuration produced the best result, the chine case refers to the Chine#3 configuration hereafter. As shown in Fig. 27a, the lift curves are very similar for all three cases in the linear region ($\alpha < 12°$). The slope change (i.e., lift reduction) for the baseline case is due to the existence of the nacelle/pylon wake and its associated flow separation. Applying a nacelle chine recovered the performance of the wing especially near the C_{Lmax} region producing a comparable lift curve to that of the NNP case. This indicates that the application of the nacelle chine reduces the adverse effects of the nacelle/pylon wake. The nacelle chine maintained the slope of the lift curve until C_{Lmax}. In addition, C_{Lmax} was increased by approximately 0.06 using the nacelle chine. For the poststall ($\alpha > 16.5°$) conditions, the nacelle chine was unable to reduce the effect of the wake; therefore, the drop in the lift curve was more severe than that of the NNP case. The poststall C_L value is comparable to the baseline case rather than the NNP case as the nacelle chine loses its effectiveness. Similarly, the nacelle chine recovered the linear relationship between C_D and C_L^2 by eliminating the performance degradation near C_{Lmax} (Fig. 27b). The performance improvement results in a less drag for the same lift values near C_{Lmax}. The NNP case also has a linear relationship until C_{Lmax} but as mentioned before, the NNP curve is shifted to the right clearly demonstrating substantially lower profile drag as expected. In addition, the slope is slightly smaller than that of the baseline case indicating that the effect of a nacelle on the drag increases with angle of attack.

Figure 28 presents the near stall (at $\alpha = 16°$) C_p distributions for the baseline, chine, and NNP cases inside ($y = 27.8$ in.) and outside ($y = 63.8$ in.) the wake region. Inside the wake region, the NNP case produces the highest suction pressures on both the main wing and the flap compared to the baseline and the chine cases (Fig. 28a). The pressure recovery on the flap is comparable to that of the nacelle chine case indicating that the nacelle chine not only reduces the flow separation on the main wing but also improves the pressure recovery on the flap by maintaining attached flow (Fig. 28a). As expected, all three cases produce almost identical C_p distributions outside the wake region (Fig. 28b).

The surface tuft visualization in Fig. 29 demonstrates the effectiveness of the nacelle chine at $\alpha = 16°$ when compared to the baseline case in Fig. 10. As clearly shown, the nacelle chine is able to eliminate the flow separation shown in Fig. 10 near the main wing trailing edge. The tufts exhibit unsteady flow over the main wing downstream of the pylon without any sign of separated flow (Fig. 29). Consistent with the C_p distribution in Fig. 28a, flow separation control over the main wing also affects the flow over the inboard flap where the tufts appear to be more streamlined due to the attached flow. Outside the nacelle-wake region, the surface flow visualization is similar to the baseline case shown in Fig. 10 and Fig. 12a.

At the poststall condition (at $\alpha = 18°$), the lift curve in Fig. 27a does not indicate any benefit of using the nacelle chine. However, the tuft flow visualization results in Fig. 30 show noticeable differences for the overall flow topology. This can be seen when the baseline (in Fig. 11) and chine (Fig. 30) cases are compared side by side. For the baseline case, flow separation is triggered by the nacelle/pylon wake; therefore, it is primarily concentrated in the region downstream of the nacelle/pylon with a wing-body separation bubble near the main wing trailing edge (Fig. 11). However, for the chine case (Fig. 30), flow separation is dominated by the wing-body separation bubble, where the separated flow is concentrated over the inboard side of the main wing in the vicinity of the fuselage. This flow separation spans almost the entire chord and extends to the midspan of the inboard wing (Fig. 30). Although the nacelle/pylon wake still exists (see unsteady tufts downstream of the pylon), the flow appears to be attached. It is apparent that the nacelle chine reduced the adverse effect of the nacelle/pylon wake; however, it might also promote flow separation on the most inboard section. This is because the nacelle chine has a skew angle that generates a counterclockwise rotating streamwise vortex (when looking downstream). Therefore, the downwash region of the nacelle chine vortex is on the outboard side; whereas, the upwash region of the vortex is on the inboard side of the wing as depicted on the figure (Fig. 30). At the downwash side, the vortex brings high momentum fluid to the wing surface; therefore, it reduces the boundary layer thickness. On the upwash side, the vortex increases the boundary layer thickness and makes the boundary layer more prone to separation.

D. Numerical Simulations

Computational Fluid Dynamics (CFD) simulations were performed for select cases to aid in understanding the flow structures that developed on the CRM-HL model. Numerical simulations are especially useful when considering the complete 3D flow field with many variables provided by CFD. In this study, the CFD results are deemed qualitative

in nature and are complementary to the experimental results. A rudimentary comparison is provided to point out the agreements/disagreements between the experimental and numerical flow visualizations, but a quantitative comparison of the numerical results with the experimental data will be the subject of another study. Before presenting the results at near stall (at $\alpha = 16°$) and poststall (at $\alpha = 18°$) conditions, where the nacelle/pylon wake becomes dominant, the numerical results for the nominal approach angle ($\alpha = 8°$) will be presented first as a reference. The vortical structures generated by the various parts of the CRM-HL model are shown in Fig. 31. The vortices were identified by the λ_2 isosurfaces and colored by the nondimensional streamwise vorticity to show the vorticity direction. Although similar vortical structures were shown in the literature previously [16-17], the results presented in this study are more representative of a commercial airplane. The pylon/wing region is complex, and several vortices are shed from this complex geometrical structure. As shown in Fig. 31, the outboard slat generates a negative (counterclockwise, when looking downstream) vortex and the outboard cutout generates a positive (clockwise) vortex. The vortex sign reverses on the inboard side where the slat generates a positive vortex and the cutout generates a negative vortex. In addition, there are two vortices generated by the pylon. The first one is generated at the pylon shoulder. This vortex is negative (counterclockwise) sign and shed to the upper surface of the wing over the slat cutout. The second vortex is generated at the junction between the engine nacelle and pylon and shed to the lower surface of the wing. Near the wing/fuselage junction, the slat generates a negative vortex and the leading-edge strake generates a positive vortex that are shed to the upper surface of the wing. The leading-edge strake generates another vortex at the fuselage junction that is shed to the lower surface of the wing.

Total pressure, C_{Pt}, contours at several streamwise sections are presented in Fig. 32 for $\alpha = 8°$. The negative total pressure values indicate total pressure (i.e., energy) losses that are mainly due to the wake (off the surface) and viscous effects (near wall). As shown in this figure, the vortex pair on the outboard side of the slat cutout merge and convect downstream. Although the off-surface wake diminishes downstream as the vortex expands, the signature of the vortex on the boundary layer persists all the way to the trailing edge. There is a large low-energy region downstream of the slat cutout that is caused by the vortices generated by the pylon and the outboard side of the inboard slat. At this angle of attack, the adverse pressure gradient (APG) on the main wing is not severe; therefore, the off-surface wake dissipates naturally as it expands, but its footprint on the boundary layer persists downstream. The vortex generated by the inboard side of the slat cutout is also shown in the figure. This vortex is weak and dissipates quickly. Another weak vortex is seen near the fuselage that is generated by the leading-edge strake and by the most inboard slat. The total pressure contours also demonstrate the wakes generated by the slat brackets. Because the slat bracket wakes are generated near the leading edge of the main wing, they are exposed to a favorable pressure gradient, and; therefore, they are embedded in the boundary layer.

Figure 33 illustrates the surface flow visualization predicted by the numerical simulations. In this figure, the surface streamlines are superpositioned on the transverse velocity fluctuation, U'_n, contours. Overall, the flow appears to be attached over most of the model except for the flap surfaces. The nacelle/pylon wake is weak and confined to the slat cutout region. The wakes generated by the slat brackets are easily identified by the velocity fluctuations. The magnitude of the velocity fluctuations due to slat bracket wakes is initially high then appears to diffuse gradually over most of the regions except for the aileron section. In the aileron region, the magnitudes of the fluctuations first diffuse but then increase near the trailing edge. The CFD results indicate local 3D flow separation on the inboard flap near the trailing edge, which was not shown in the tuft flow visualization in Fig. 8. On the other hand, the entire outboard flap is dominated by 3D flow separation that is consistent with the tuft flow visualization (Fig. 12a). The separation bubble between the inboard flap and the fuselage was captured. The higher U'_n levels upstream of the flap fairings in Fig. 33 indicate unsteady/separated flow that agrees with the flow unsteadiness observed by the tufts in Fig 8.

At the near stall condition ($\alpha = 16°$), the vortex structures appear similar to those of the $\alpha = 8°$ case with two minor differences (Fig. 34a). The first difference is that the pylon vortex splits into two; one generated at the pylon shoulder and the other generated at the pylon/nacelle junction. The other difference is the vortex generated at the outboard side of the inboard slat that moved toward the inboard side. Installing a nacelle chine, which is the Chine#3 configuration in the experiment, does not change the other vortical structures except the one it generates. As expected, the nacelle chine generates a strong streamwise vortex that has a negative sign (counterclockwise rotating) due to the chine's skew angle with respect to incoming flow (Fig. 34b).

Figure 35a shows the total pressure contours at several streamwise sections for the near stall condition (at $\alpha = 16°$). When compared to the nominal approach angle ($\alpha = 8°$) in Fig. 32, there are substantial total pressure losses on the nacelle upper surface. The loss in the total pressure is caused by the flow separation on the nacelle upper surface, which did not exist at $\alpha = 8°$. In addition, the nacelle/pylon wake, which comprises the vortices generated by the pylon, inboard slat cutout and outboard side of the inboard slat, has a trajectory that is biased toward the inboard side. As a result, the wake near the leading edge is stronger than that of the $\alpha = 8°$ case. At this angle of attack, the APG on the main wing is more severe than that of the $\alpha = 8°$ case; therefore, these low energy regions continually grow

9

downstream. This statement holds true for all the vortices except for the vortex pair generated near the fuselage. Although the pressure loss region is considerably larger than that of the $\alpha = 8°$ case, the off-surface wake dissipates downstream, but its footprint on the boundary layer grows similar to the other vortices.

The effect of the nacelle chine and its generated vortex is evident when the total pressure contours of the baseline and chine cases are compared (Figs. 35a and b). The streamwise vortex generated by the nacelle chine travels downstream along the inboard side of wing. The vortex is off the surface but its footprint on the near wall region is also shown in the figure. The chine vortex is strong enough that its wake persists past the trailing edge. The total pressure contours indicate that the wake near the leading edge of the slat cutout is weaker than that of the baseline case when the nacelle chine is used. The main effect of the chine vortex is that it reduces the growth of the nacelle/pylon wake on the main wing. Therefore, compared to the baseline case (Fig. 35a), the extent of the nacelle/pylon wake is considerably reduced when the nacelle chine is used (Fig. 35b). In addition, the pressure loss near the leading edge of the nacelle is shown to shrink slightly indicating that the nacelle chine also reduces the flow separation on the nacelle upper surface compared to the baseline case. As shown in this figure, the vortices generated by the outboard slat/cutout, leading edge strake, and slat brackets appear similar to the those of the baseline case.

Surface flow visualization predicted by the CFD simulation is presented for the baseline case at the near stall conditions (Fig. 36a). At this angle of attack ($\alpha = 16°$), the surface streamlines indicate separated flow over the nacelle upper surface, which explains the total pressure loss that was observed in Fig. 35a. Note that the flow separation on the nacelle upper surface did not exist in the limited tuft flow visualization in the experiments. The effect of the nacelle/pylon wake is more pronounced compared to that of the nominal approach angle ($\alpha = 8°$) in Fig. 33. The wake causes more unsteady flow, affecting a larger area on the inboard main wing as shown by the high U'_n regions (Fig. 36a). As a result, the surface streamlines indicate flow separation near the trailing edge of the inboard wing. The separated flow region qualitatively agrees with the experiment but is predicted to be smaller in the simulations. The inboard flap experiences higher velocity fluctuations. The complex interactions between the separated flow, nacelle/pylon wake, the flow from the flap slot, and the APG due to the flap deflections are the reasons for the high velocity fluctuations on the inboard flap. Zooming in to the inboard flap region shows attached flow in the numerical simulations; whereas, the tuft flow visualization in Fig. 10, as well as the C_p distribution in Fig. 28, indicated flow separation for the baseline case for $\alpha = 16°$. Similar disagreement between the CFD and tuft flow visualization results can also be seen on the outboard wing, where CFD predicted less spanwise flow and no 3D flow separation (compare Fig. 36a to Fig. 12b). The local flow separation observed in the tuft flow visualization on the aileron section in Fig. 12b is successfully predicted by the numerical simulations (Fig. 36a). These local flow separation regions are downstream of the slat brackets and caused by the interaction of the slat bracket wakes with the APG. When compared to the nacelle chine case, the surface flow visualization predicted by the CFD simulations clearly shows the effect of nacelle chine (Fig. 36b). The nacelle/pylon wake is reduced (compare U'_n levels to Fig. 36a) and flow separation on the inboard wing is eliminated. Consequently, the velocity fluctuations over the inboard flap are also reduced. In addition, the flow separation bubble on the nacelle upper surface is reduced slightly. For the rest of the regions (i.e., outboard wing, outboard flap, aileron section, and fuselage), the flow appears similar to the baseline case, as expected.

The trends in the CFD predictions are the same when the angle of attack is increased further to the poststall condition (at $\alpha = 18°$). As shown in the total pressure contours (Fig. 37a), the nacelle/pylon wake grows substantially, causing more energy loss. The nacelle chine generates a strong streamwise vortex that persists past the trailing edge (Fig. 34b). At this angle of attack, the APG is severe and the chine vortex could not eliminate the growth of the nacelle/pylon wake. However, the chine vortex reduces the nacelle/pylon wake considerably, when compared to the baseline case. Note that the chine vortex has a negative sign (counterclockwise rotating) where the downwash region is on the outboard side and upwash region is on the inboard side. Despite the chine vortex and its evident effect on the wake, the benefit of using a nacelle chine at poststall ($\alpha = 18°$) is negligible (Fig. 27a). This is because while the chine vortex reduces the nacelle/pylon wake over the downwash region, it also increases the boundary layer thickness over the upwash region, hence increasing the energy loss near the wing/fuselage juncture. This is clearly seen when the total pressure contours near the wing/fuselage juncture for the baseline and chine cases are compared. This agrees very well with the experimental results where the separated flow region is concentrated mostly downstream of the nacelle/pylon for the baseline case (Fig. 11) and near the wing/fuselage juncture for the chine case (Fig. 30).

Figure 38 illustrates the surface flow visualization predicted by the CFD simulations for the poststall (at $\alpha = 18°$) condition. Compared to the near stall condition (at $\alpha = 16°$), the nacelle/pylon wake becomes stronger and affects most of the inboard wing. The separated flow region near the midspan of the inboard wing extends upstream covering most of the inboard wing. In addition to this region, the surface streamlines indicate another region of separated flow upstream of the Yehudi break near the main wing trailing edge (Fig. 38a). The stronger wake also affects the flow over the inboard flap (higher U'_n levels in Fig. 38a); however, zooming in to this region shows that the streamlines are almost straight (i.e., attached flow) in the numerical simulations. No noticeable difference is observed on the outboard

flap compared to the near stall conditions where the flow is unsteady but attached. A considerable effect of the nacelle chine is shown in the surface flow visualization (Fig. 38b). The fluctuating velocity magnitudes undoubtedly indicate the reduction of the nacelle/pylon wake both on the main wing as well as on the inboard flap. The flow separation near the main wing trailing edge still exists, but its size is considerably reduced. The flow separation near the Yehudi break is eliminated. Although the total pressure contours showed the effect of the nacelle chine near the wing/fuselage juncture, the large wing-body separation bubble observed in the tuft visualization (Fig. 30) was not predicted by the CFD simulations.

V. Conclusion

A 10% scale version of the High-Lift Common Research Model (CRM-HL) was successfully tested in the NASA Langley Research Center 14- by 22-Foot Subsonic Tunnel. The CRM-HL model is representative of a modern civil transport aircraft and has all the details including fuselage, nacelle, pylon, a single-slotted Fowler flap, flap fairings, slat, slat brackets, etc. The modular design enabled the testing of the CRM-HL model with and without an engine nacelle. Wind tunnel measurements included force and pressure data as well as surface flow visualization with minitufts. For select cases, numerical simulations were also performed to aid in understanding the wind tunnel data.

The present study investigates the wake generated by various parts of the CRM-HL model, especially by the nacelle/pylon. First, for the baseline case, defined as the CRM-HL configuration with nacelle/pylon, aerodynamic force measurements indicated performance degradation at higher angles of attack prior to stall. Tuft flow visualizations displayed the nacelle/pylon wake as flow unsteadiness at lower angles of attack. The nacelle/pylon wake became stronger as the angle of attack was increased and triggered flow separation on the inboard wing. This flow separation and associated wake also affected the flow over the inboard flap. The slat bracket wake accounted for the local flow separation over the aileron section. The local flow separation is caused by the interaction of the slat bracket wake and the adverse pressure gradient.

In order to isolate the nacelle/pylon effect, the wind tunnel experiments were repeated without the engine nacelle/pylon. The no nacelle/pylon (NNP) configuration was designed to have a continuous slat/WUSS. Therefore, this configuration not only eliminated the nacelle/pylon wake but also provided a continuous slat gap. Surface flow visualization with minitufts showed attached flow for both the near stall ($\alpha = 16°$) and poststall ($\alpha = 18°$) conditions where the baseline cases showed a large flow separation bubble. Elimination of the nacelle and its associated wake maintained attached flow over the inboard flap. The NNP case provided higher suction pressures over the inboard wing and inboard flap, where the nacelle/pylon wake is more pronounced. The induced drag characteristics of the NNP case showed three distinct features. First, the curve has a linear relationship until C_{Lmax}. Second, the curve is shifted to the right clearly showing that the NNP case produces substantially lower drag. Third, the slope of the curve is smaller than that of the baseline case indicating that the effect of a nacelle on the drag increases with angle of attack.

A nacelle chine was used to control the flow separation caused by the nacelle/pylon wake. The nacelle chine, a type of vortex generator, was installed on the inboard side of the nacelle. By moving the nacelle chine in the circumferential location at azimuthal angles of 34°, 39°, 45°, respectively, three-different chine locations were investigated. Each chine location gradually improved the lift coefficient near C_{Lmax}. Although the application of a nacelle chine increased the drag coefficient for the same angle of attack, it was shown that the drag increase is due to the induced drag caused by flow separation control. In contrast, the induced drag characteristics clearly showed that the drag is reduced for the same lift values when flow separation was controlled with the nacelle chine. Tuft flow visualization showed that all three-chine locations eliminated the flow separation over the main wing at the near stall condition. The nacelle chine also reduced the flow separation over the inboard flap but only the best case (45° azimuthal angle location) eliminated the flow separation. This was shown in the tuft flow visualization and confirmed by the pressure distribution over the inboard flap where complete pressure recovery was achieved. This particular case was used as a benchmark for the AFC version of the CRM-HL model.

The comparison of the chine results with those of the baseline and NNP case indicated that a single nacelle chine installed on the inboard side of the engine nacelle was able to reduce the adverse effects of the nacelle/pylon wake at higher angles of attack. A properly placed nacelle chine could eliminate flow separation and provide the necessary lift recovery. This performance improvement also resulted in less drag for the same lift values near C_{Lmax}. For the poststall condition, the nacelle chine lost its effectiveness and provided aerodynamic performance similar to the baseline case. Although the nacelle chine reduced the effect of the nacelle/pylon wake and its associated flow separation over the main wing, it might also adversely affect the flow near the wing/fuselage junction at the poststall condition ($\alpha = 18°$). While the vortex generated by the nacelle chine eliminated the flow separation caused by the nacelle/pylon wake under its downwash region, it might also cause flow separation under its upwash region near the wing/fuselage juncture. As

a result, for the poststall condition, the nacelle chine could not increase the lift coefficient, but it could modify the poststall characteristics.

Finally, numerical simulations were performed to understand the flow structures that developed on the CRM-HL model. Although the focus was on the near stall and poststall conditions, the nominal approach angle ($\alpha = 8°$) for the landing configuration was also simulated to establish a reference case. The CFD simulations clearly showed the discrete vortices generated by the corners of the slat, slat cutout, pylon, leading edge strake and slat brackets. The discrete vortices generated near the slat cutout merged to form a large wake, which is called the nacelle/pylon wake. Initially, the nacelle/pylon wake was weak but became stronger as the angle of attack increased. The simulated velocity fluctuations due to the wakes compared well with the tuft unsteadiness observed in the experiment. The predicted total pressure contours clearly showed the energy loss due to the wakes and associated flow separation. The surface streamlines showed attached flow over most of the wing similar to the experiment. Both were well predicted by CFD. Overall, the CFD simulations qualitatively agreed with the experimental results for most of the regions such as capturing the unsteady flow, the 3D flow separation over the outboard flap, the flow separation generated by the nacelle/pylon wake, the local flow separation over aileron section, and the attached flow over the main wing. The disagreements between the CFD and experiments were mostly related to flow over the flaps, nacelle upper surface, and wing/fuselage juncture. The effect of the nacelle chine was also simulated and qualitatively agreed with the experiments. Although the CFD could not predict the large wing-body separation bubble near the wing/fuselage juncture at the poststall condition ($\alpha = 18°$), the total pressure contours explained the effects of the nacelle chine, and were in good agreement with the tuft flow visualization results. Overall, a combined CFD and experimental study was very helpful in understanding the flow structures and could be used to take remedial actions to improve aerodynamic performances.

Acknowledgments

References

[1] McClean, J. D., Crouch, J. D., Stoner, R. C., Sakurai, S., Feifel, G. E., Feifel, W. M., and Rush, H. M.,"Study of the Application of Separation Control by Unsteady Excitation to Civil Transport Aircraft," NASA/CR 1999–209338, 1999.

[2] Kiedaisch, J., Demanett, B., and Nagib, H., "Active Flow Control Applied to High-Lift Airfoils Utilizing Simple Flaps," AIAA Paper 2006-2856, June 2006.
https://doi.org/10.2514/6.2006-2856

[3] Melton, L. P., Schaeffler, N. W., and Lin, J. C., "High-Lift System for a Supercritical Airfoil: Simplified by Active Flow Control," AIAA Paper 2007-707, Jan. 2007.
https://doi.org/10.2514/6.2007-707

[4] Melton, L. P., Koklu, M., Andino, M., and Lin, J. C., "Active Flow Control via Discrete Sweeping and Steady Jets on a Simple-Hinged Flap," *AIAA Journal*, Vol. 56, No. 8, 2018, pp. 2961–2973.
https://doi.org/10.2514/1.J056841

[5] Lin, J. C., Melton, L. P., Viken, S. A., Andino, M. Y., Koklu, M., Hannon, J. A., and Vatsa, V. N., "High Lift Common Research Model for Wind Tunnel Testing: An Active Flow Control Perspective," AIAA Paper 2017-0319, Jan. 2017.
https://doi.org/10.2514/6.2017-0319

[6] Lacy, D. S. and Sclafani, A. J., "Development of the High Lift Common Research Model (HL-CRM): A Representative High Lift Configuration for Transonic Transports," AIAA Paper 2016-0308, June 2016.
https://doi.org/10.2514/6.2016-0308

[7] Melton, L. P., Lin, J. C., Hannon, J. A., Koklu, M., Andino, M. Y., and Paschal, K. B., "Sweeping Jet Flow Control on the Simplified High-Lift Version of the Common Research Model," AIAA Paper 2019-3726, June 2019.
https://doi.org/10.2514/6.2019-3726

[8] Lin, J. C., Melton, L. P., Hannon, J. A., Andino, M. Y., Koklu, M., Paschal, K. B., and Vatsa, V. N., "Wind Tunnel Testing of Active Flow Control on the High Lift Common Research Model," AIAA Paper 2019-3723, June 2019.
https://doi.org/10.2514/6.2019-3723

[9] Smith, A. M. O., "High-Lift Aerodynamics", *Journal of Aircraft*, Vol. 12, No. 6, 1975, pp. 501-530.
https://doi.org/10.2514/3.59830

[10] Van Dam, C. P., "The Aerodynamic Design of Multi-Element High-Lift Systems for Transport Airplanes," *Progress in Aerospace Sciences*, Vol. 38, 2002, pp. 101–144.
https://doi.org/10.1016/S0376-0421(02)00002-7

[11] Slotnick, J. and Heller, G., "Emerging Opportunities for Predictive CFD for Off-Design Commercial Airplane Flight Characteristics", Proceedings of the 54th 3AF International Conference on Applied Aerodynamics, March 1, 2019.

[12] Kerker, R. and Wells, O. "Liftvanes", US Patent 3,744,745, July 10, 1973.

[13] Haines, A. B., "Scale Effects on Aircraft and Weapon Aerodynamics", AGARD Report AG-323, July 1994.

[14] Rudnik, R., "Stall Behaviour of the EUROLIFT High Lift Configurations", AIAA Paper 2008-836, Jan. 2008.
https://doi.org/10.2514/6.2008-836

[15] von Geyr, H, van der Burg, J. W., Eliasson, P., and Esquieu, S., "CFD Prediction of Maximum Lift Effects on Realistic High-Lift Commercial Aircraft Configurations Within the European Project Eurolift II," AIAA Paper 2007-4299, 2007.
https://doi.org/10.2514/6.2007-4299

[16] Hue, D., François, C., Dandois, J., and Gebhardt, A., "Simulations of an aircraft with constant and pulsed blowing flow control at the engine/wing junction", *Aerospace Science and Technology*, Vol. 69, 2017, pp. 659-673.
https://doi.org/10.1016/j.ast.2017.07.031

[17] Fricke, S., Ciobaca, V., Kröhnert, A., Wild, J., and Blesbois, O.,"Active Flow Control Applied at the Engine-Wing Junction," 5th CEAS Air and Space Conference, CEAS Paper 249, Delft, The Netherlands, 2015.

[18] Kato, H., Watanabe, S., Murayama, M., Yokokawa Y., and Ito, T., "PIV Investigation of Nacelle Chine Effects on High-Lift System Performance," AIAA Paper 2008-240, Jan. 2008.
https://doi:10.2514/6.2008-240

[19] Kanazaki, M., Yokokawa, Y., Murayama, M., and Ito, T., "Efficient Design Exploration of Nacelle Chine Installation in Wind Tunnel Testing," AIAA Paper 2008-0155, Jan. 2008.
https://doi.org/10.2514/6.2008-155

[20] The 3rd AIAA CFD High Lift Prediction Workshop, April 2019.
https://hiliftpw.larc.nasa.gov/Workshop3/testcases.html.

[21] Gentry, G. L., Quinto, F. P., Gatlin, G. G., and Applin, Z. T., "The Langley 14 - by 22-Foot Subsonic Tunnel," NASA TP-3008, 1990.

[22] Koklu, M., Lin, J. C., Melton, L. P., Hannon, J. A., Andino, M. Y., Paschal, K. B., and Vatsa, V. N., "Surface Flow Visualization of the High Lift Common Research Model," AIAA Paper 2019-3727, June 2019.
https://doi.org/10.2514/6.2019-3727

[23] Vassberg, J. C., DeHaan, M. A., Rivers, S. M., and Wahls, R. A., "Development of a Common Research Model for Applied CFD Validation Studies," AIAA Paper 2008-6919, Aug. 2008.
https://doi.org/10.2514/6.2008-6919

[24] Chen, S. and Doolen, G., "Lattice Boltzmann Method for Fluid Flows," *Annual Review of Fluid Mechanics*, Vol. 30, 1998, pp. 329–364.
https://doi.org/10.1146/annurev.fluid.30.1.329

[25] Teixeira, C., "Incorporating Turbulence Models into the Lattice-Boltzmann Method," International Journal of Modern Physics, Vol. 9, 1998, pp. 1159–1175.
https://doi.org/10.1142/S0129183198001060

[26] Vatsa, V., Duda, B., Lin, J., Melton, L., and O'Connell, M., "Numerical Simulation of a Simplified High-Lift CRM Configuration Embedded with Fluidic Actuators," AIAA Paper 2018-3063, June 2018.
https://doi.org/10.2514/6.2018-3063

[27] Barlow, J. B., Rae, W. H., and Pope, A., "Low-Speed Wind Tunnel Testing", New York: Wiley, 1999.

[28] Crowder, J. P., "Tufts", in Handbook of Flow Visualization, 2nd Edition. Yang, W.-J. (Ed) pp. 131-179, CRC Press, New York, 2001.
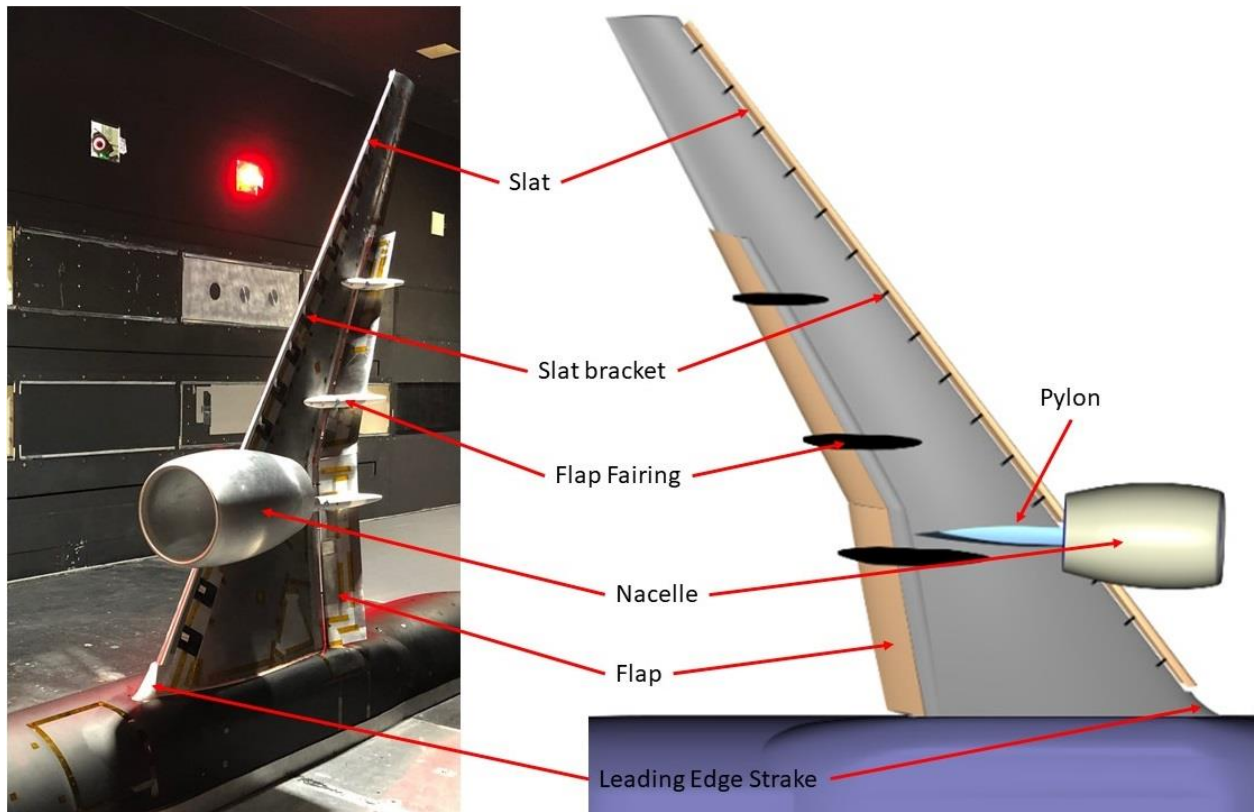
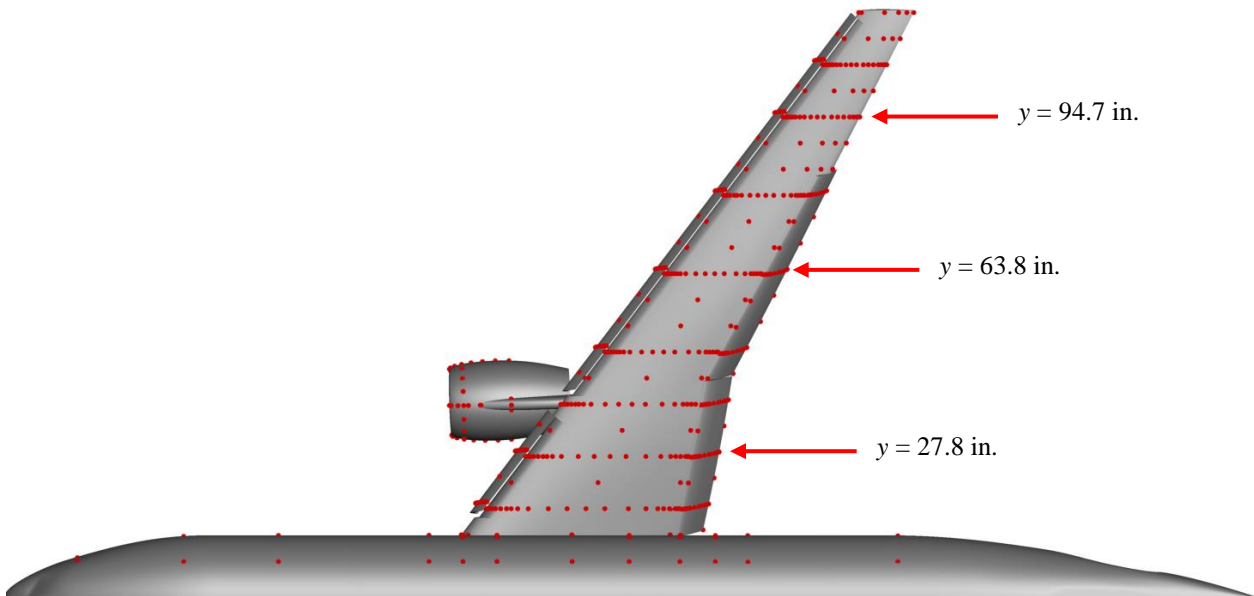**Fig. 1 Conventional CRM-HL model installed in the 14x22 tunnel and its CAD rendering.**

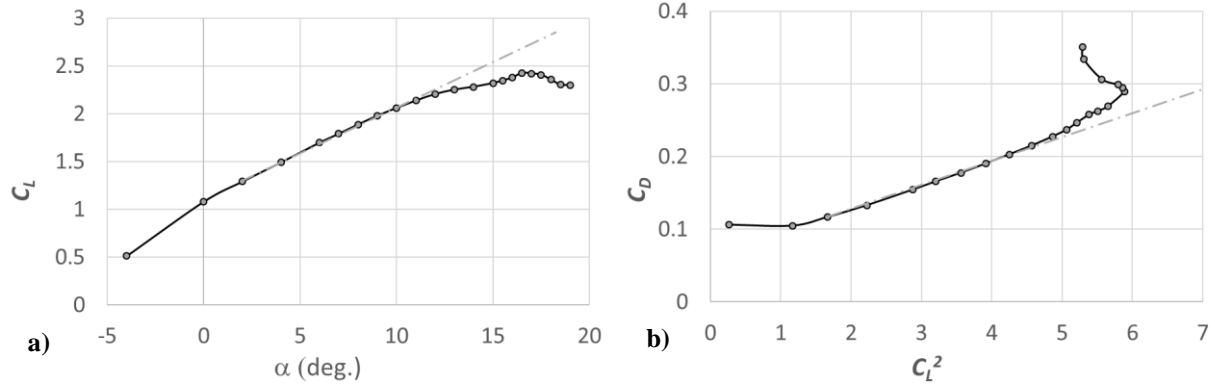**Fig. 2 Schematic of the surface pressure port locations on the CRM-HL model.**

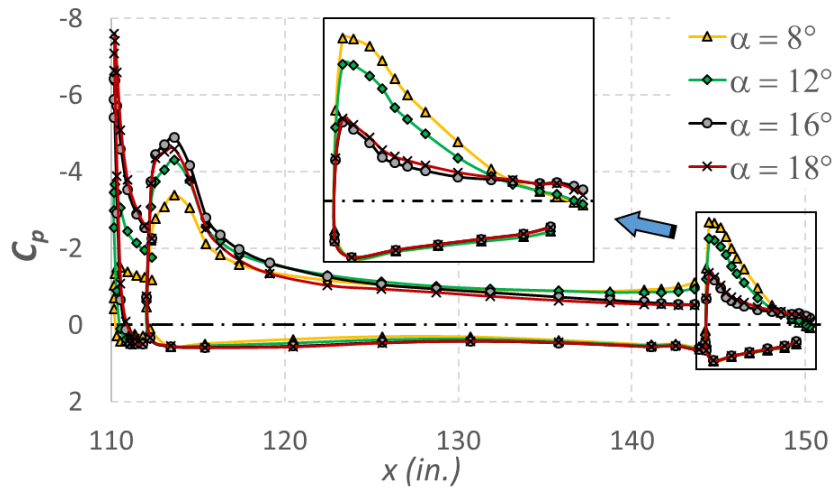**Fig. 3 Aerodynamic performance of the baseline CRM-HL model: a) lift coefficient, b) induced drag.**

Fig. 4 Streamwise C_p distributions for the baseline case (inboard section, y = 27.8 in.).
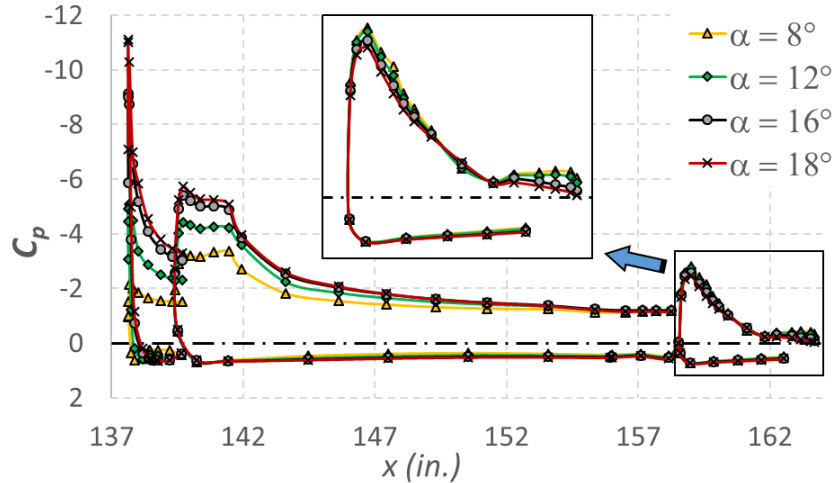

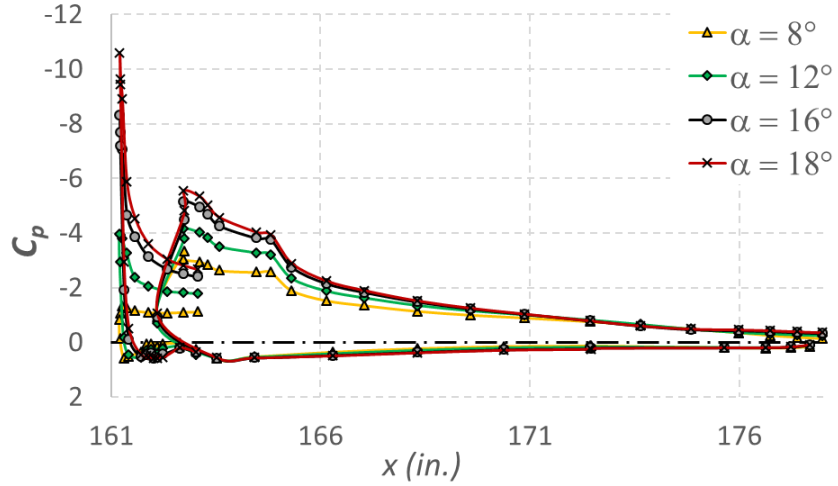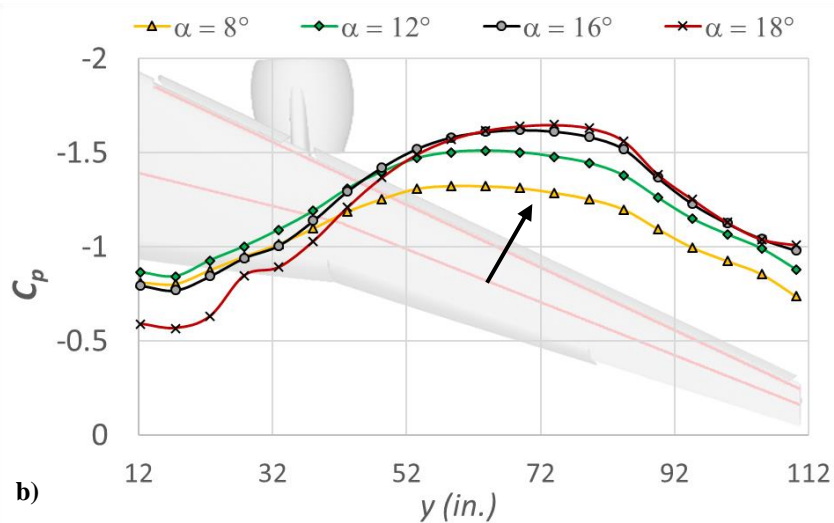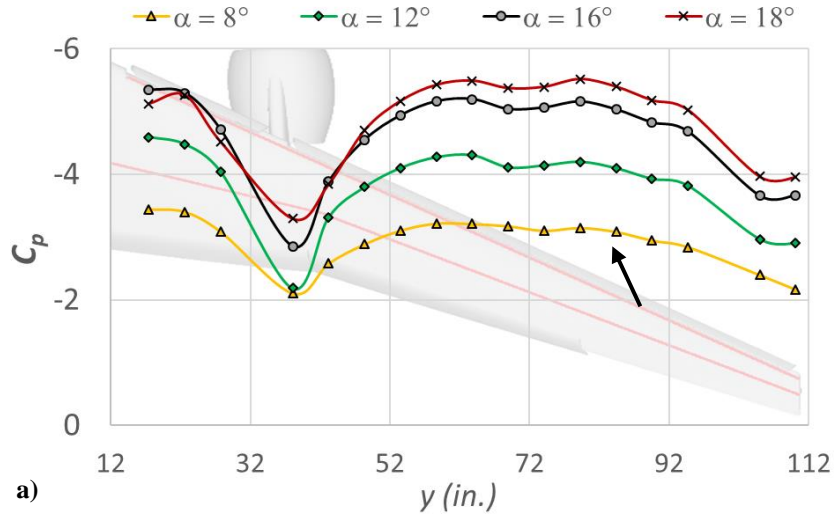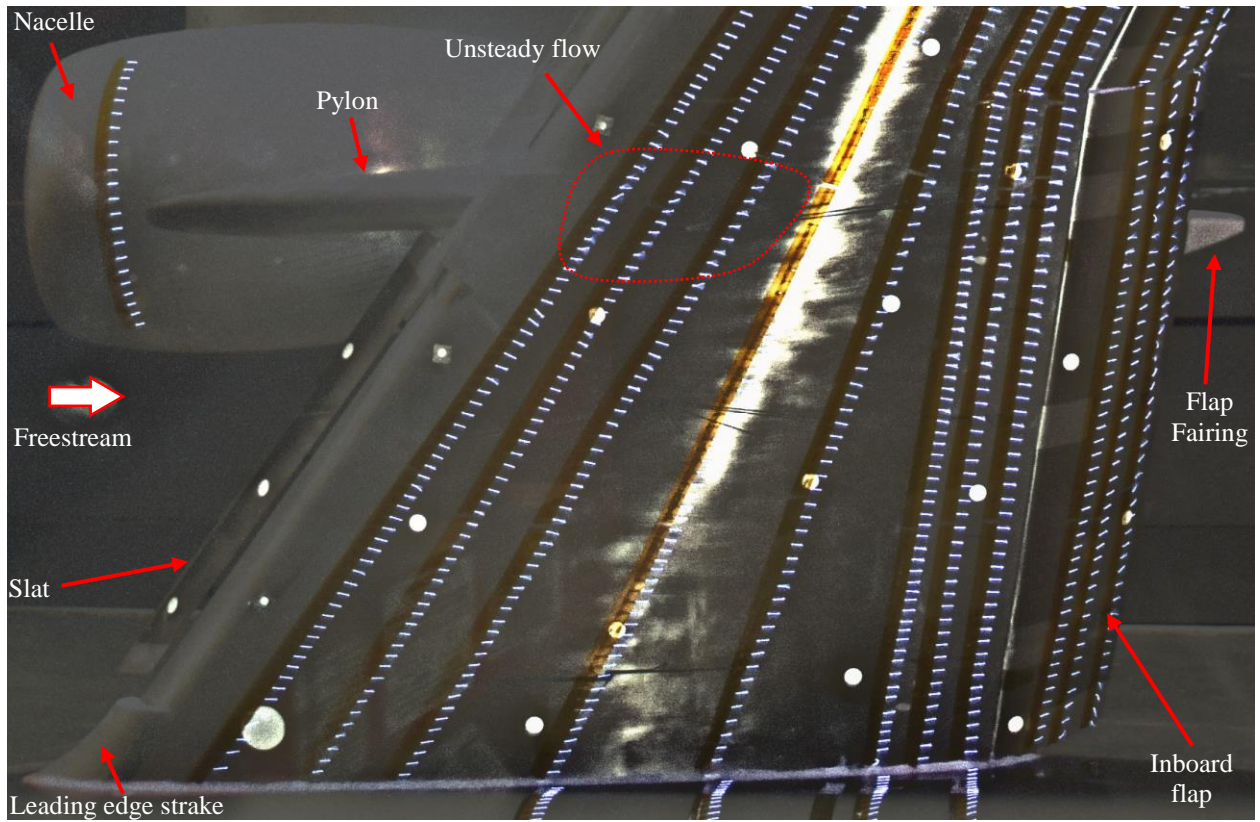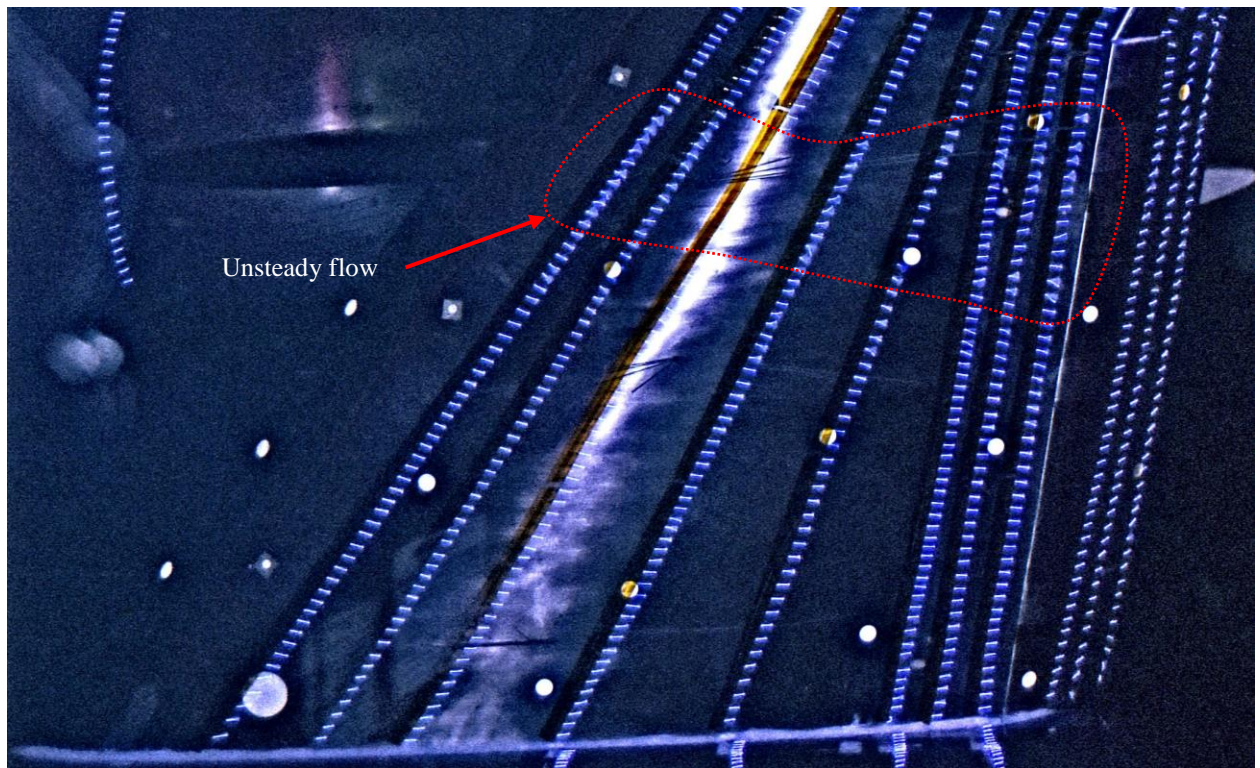**Fig. 5 Streamwise C_p distributions for the baseline case (midboard section, y = 63.8 in.).**

Fig. 6 Streamwise C_p distributions for the baseline case (outboard section, y = 94.7 in.).

a)

b)

Fig. 7 Variation of the spanwise C_p distribution with α: a) near the leading-edge, b) along the midchord.

Fig. 8 Surface tuft flow visualization of the baseline case at α = 8°.

Fig. 9 Surface tuft flow visualization of the baseline case at α = 12°.
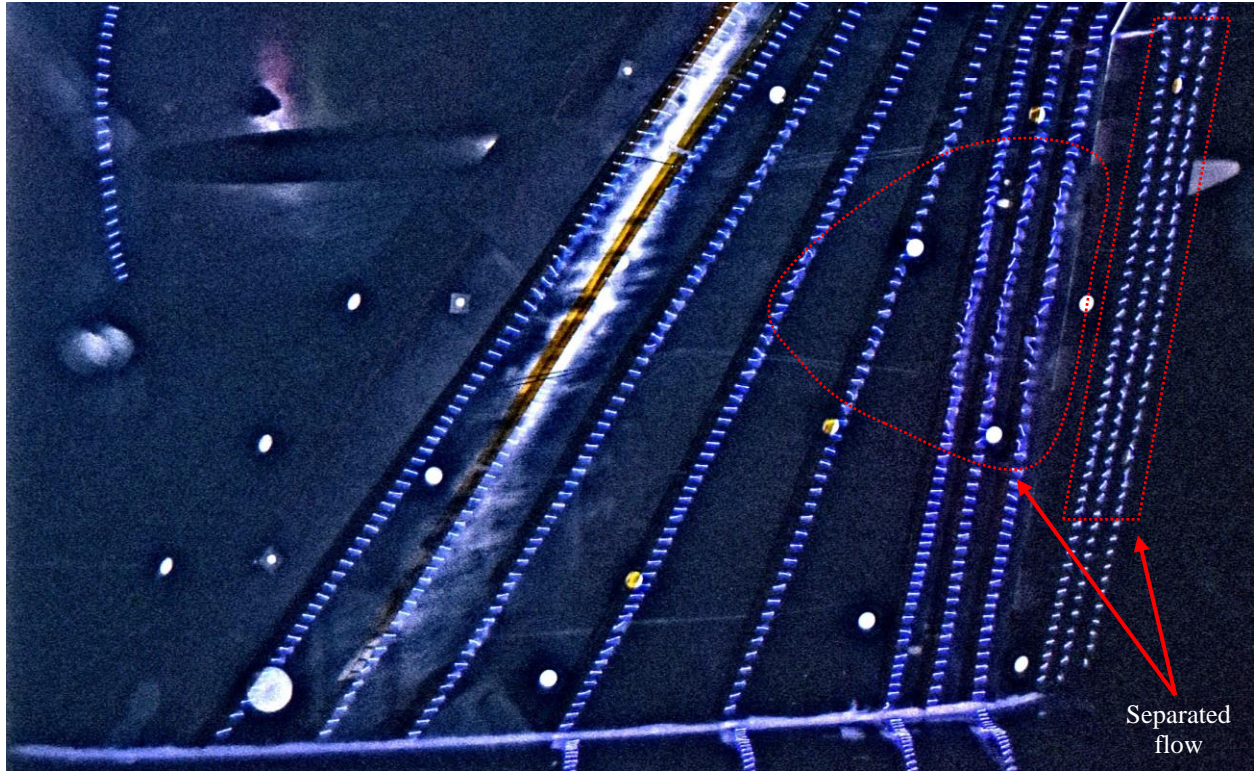
Fig. 10   Surface tuft flow visualization of the baseline case at α = 16°.
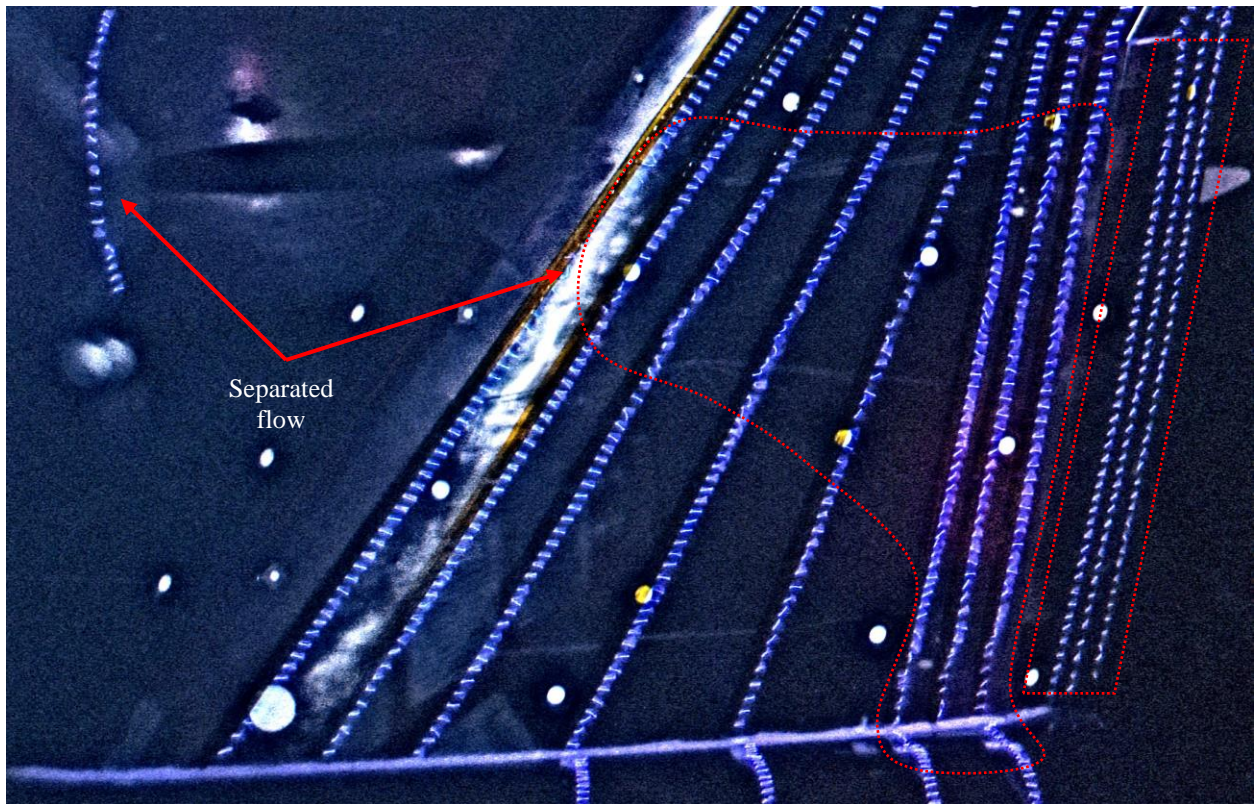
Fig. 11   Surface tuft flow visualization of the baseline case at α = 18°.
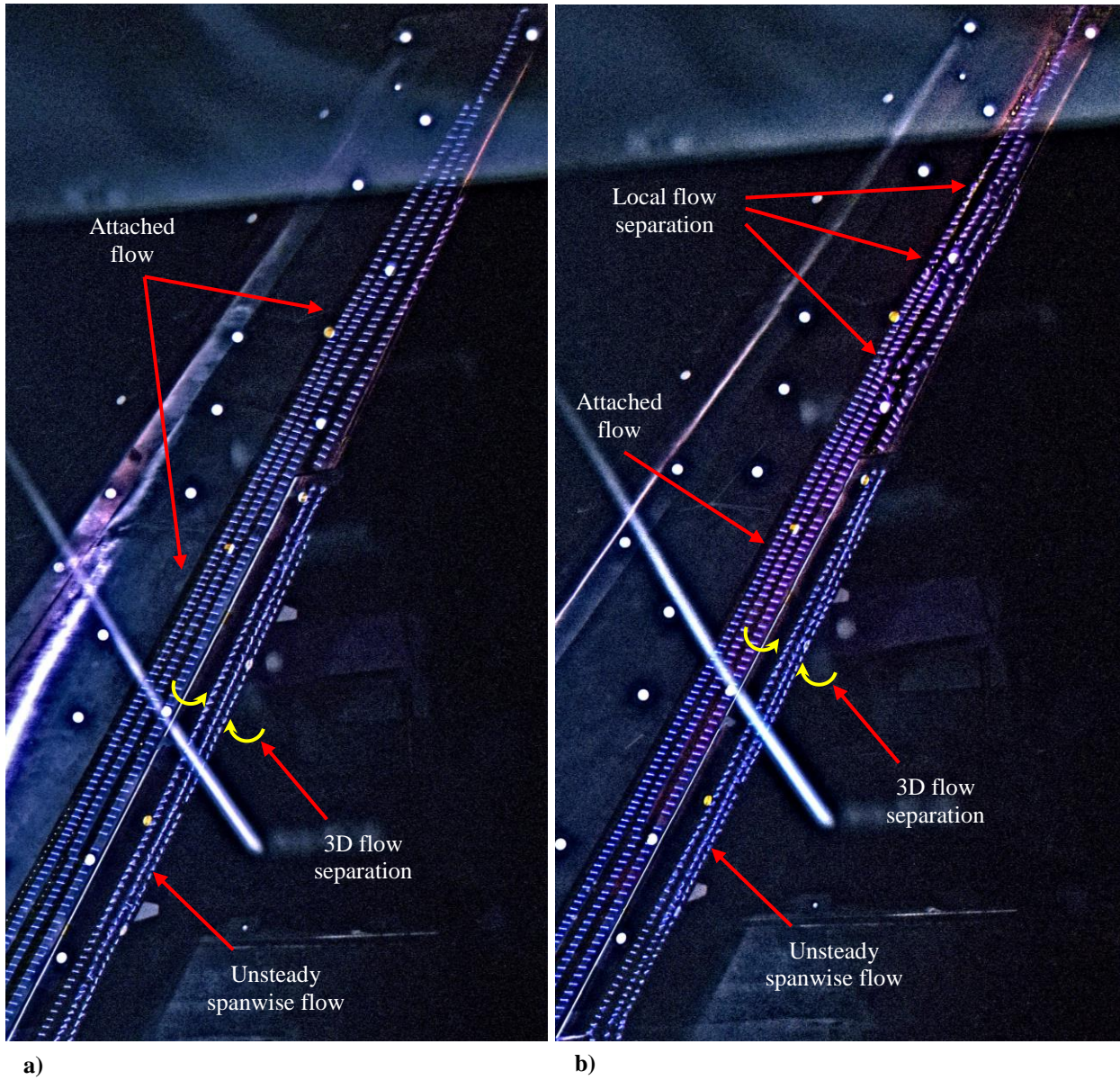
Fig. 12   Surface tuft flow visualization for the outboard wing: a) α = 8°, b) α = 16°.

a)   b)

Fig. 13   The CRM-HL model in the 14x22 without the nacelle/pylon: a) upper surface, b) lower surface.

a)   b)
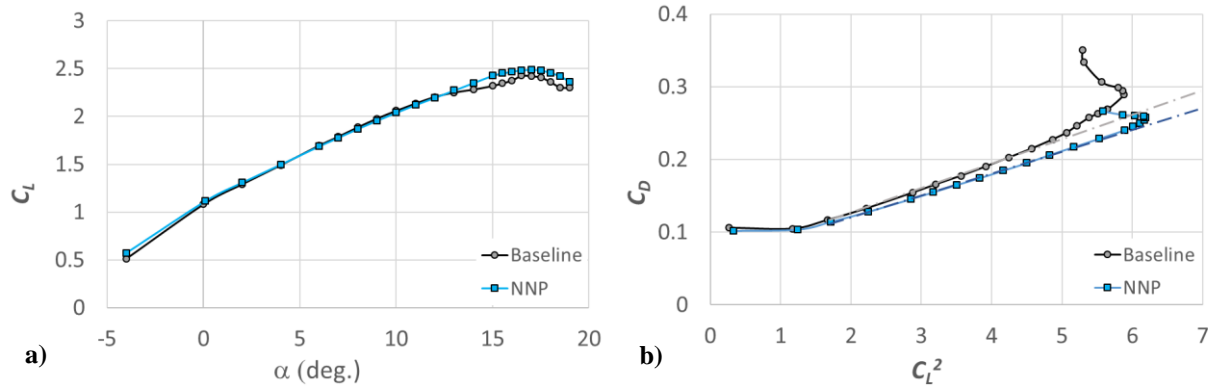
Fig. 14   Comparison of the baseline and NNP cases: a) lift coefficient, b) induced drag.
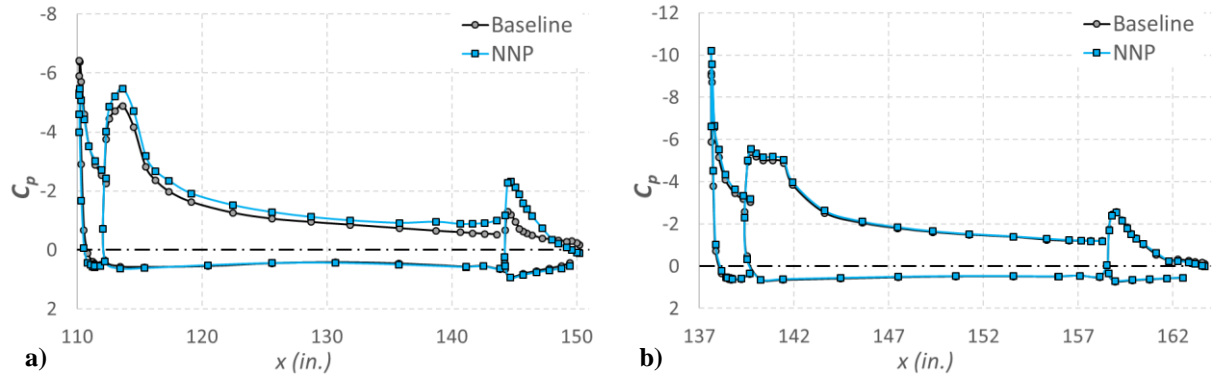
Fig. 15   Streamwise C_p distributions for the baseline and NNP cases ($\alpha = 16°$): a) $y = 27.8$ in., b) $y = 63.8$ in.
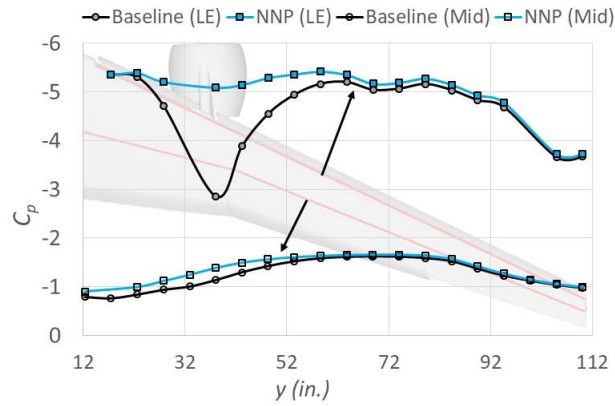
Fig. 16   Spanwise C_p distributions for the baseline and NNP cases ($\alpha = 16°$).
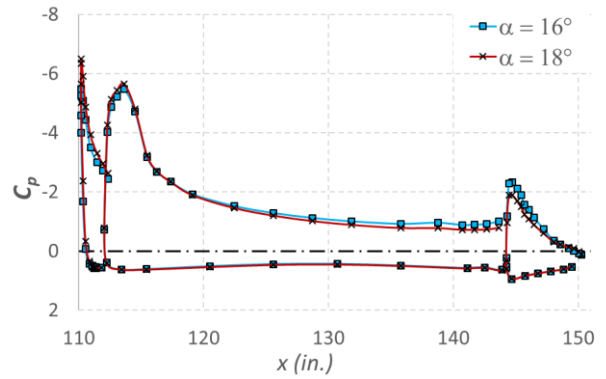
Fig. 17   Streamwise C_p distributions at near stall and poststall conditions (NNP case, $y = 27.8$ in.).

21
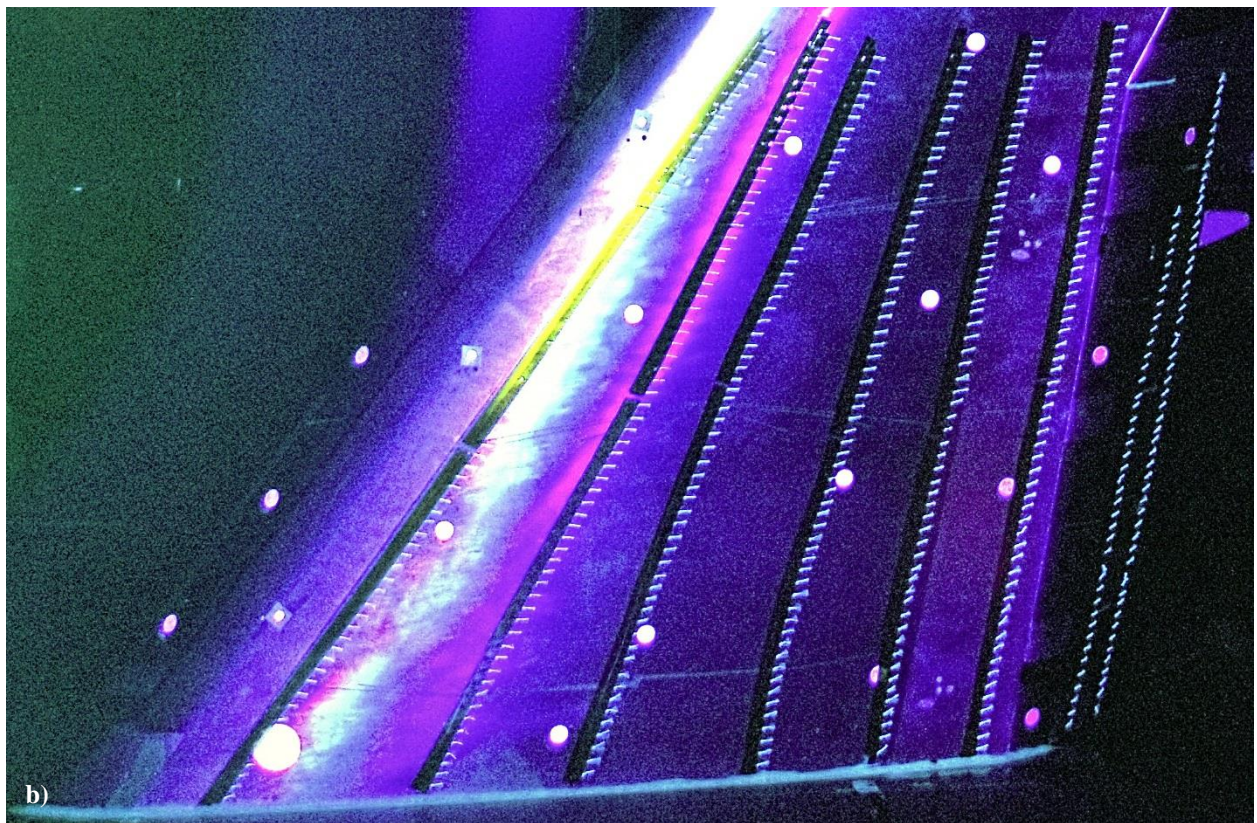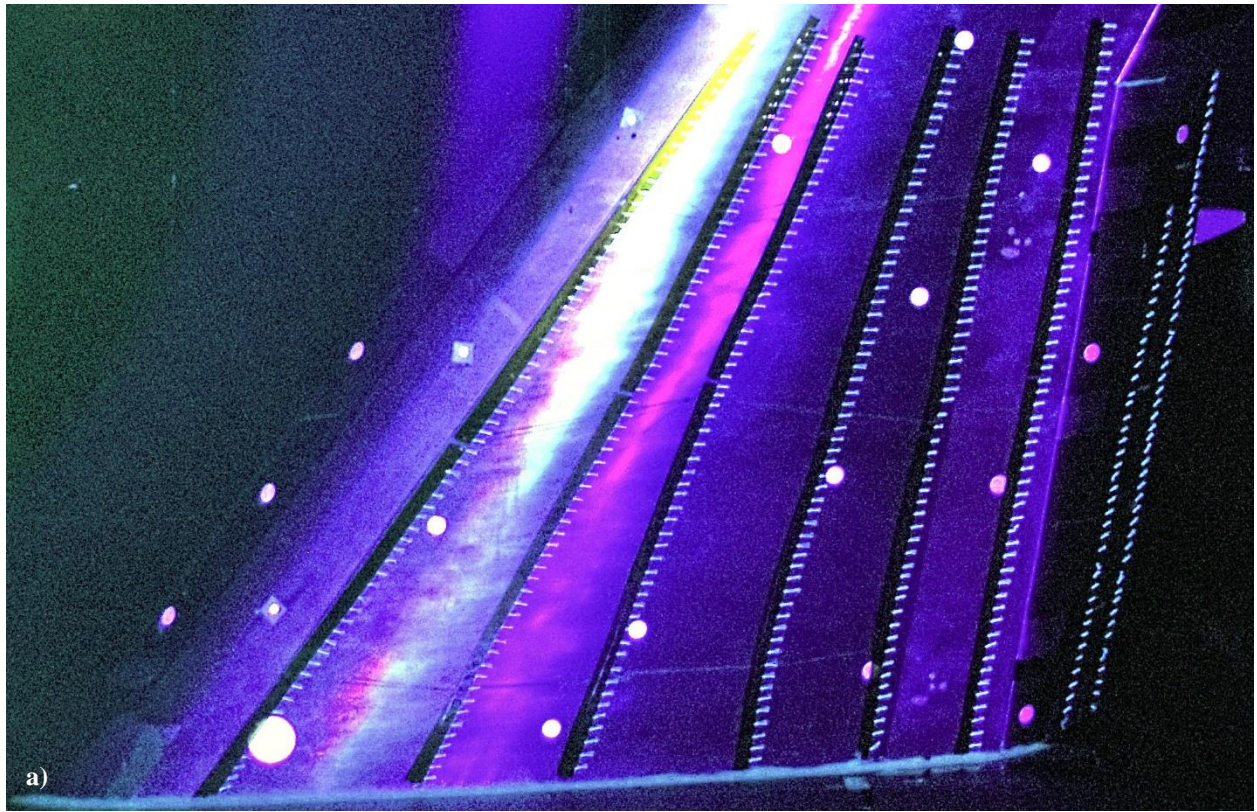
Fig. 18   Surface tuft flow visualization for the NNP case: a) α = 16°, b) α = 18°.

<div align="center">

a)   b)
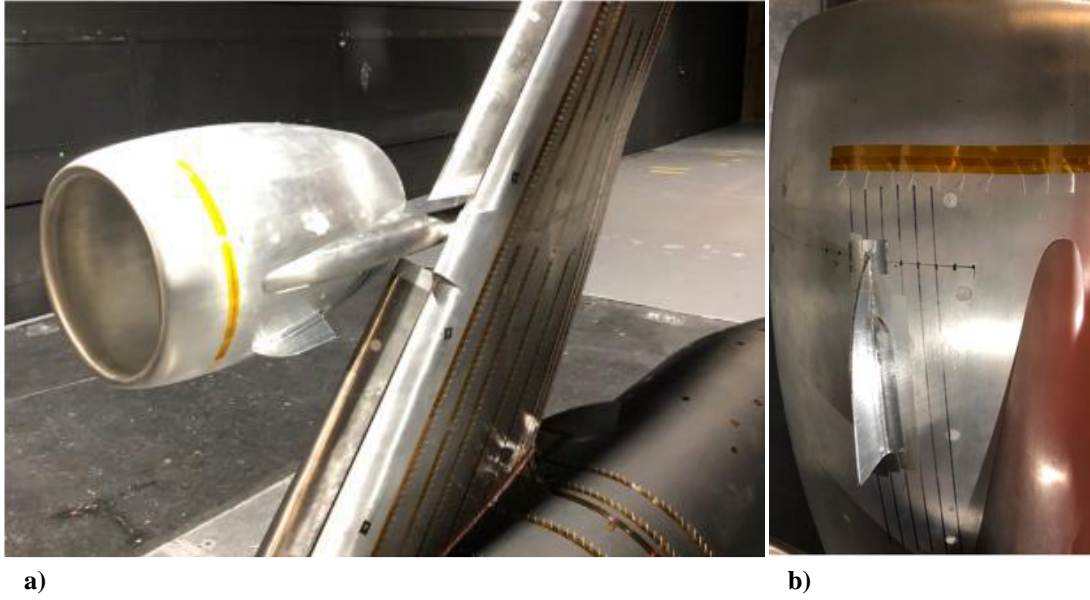
Fig. 19   Nacelle chine used on the CRM-HL Model: a) nacelle chine installed on the model, b) close-up view.

</div>

<div align="center">

a)   b)
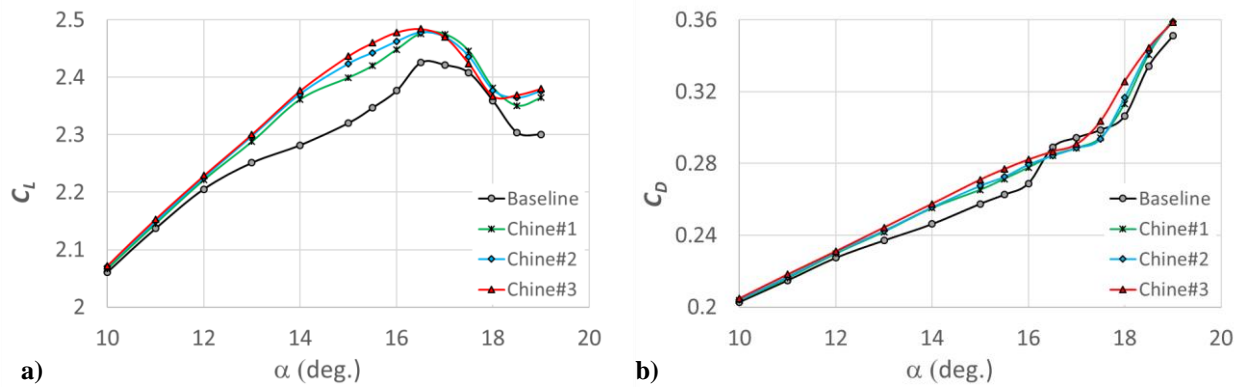
Fig. 20   Variation of a) lift, and b) drag coefficients for different chine configurations.

</div>

<div align="center">
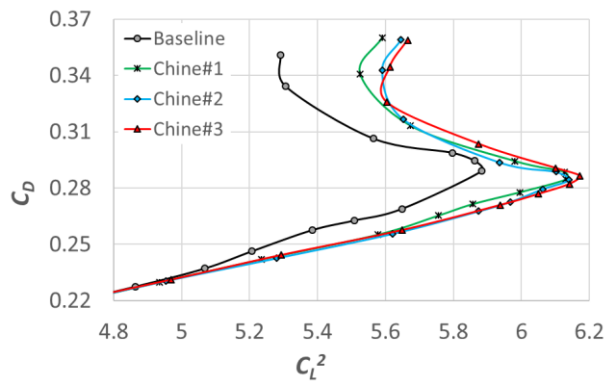
Fig. 21   Induced drag characteristics of different chine configurations.

</div>

<div align="center">
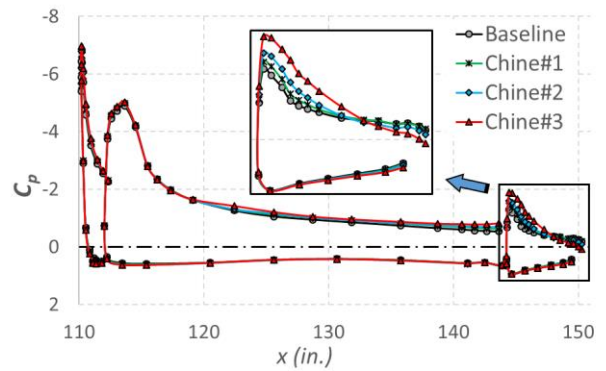
Fig. 22 Streamwise C_p distributions for different chine configurations (y = 27.8 in., α = 16°).

</div>
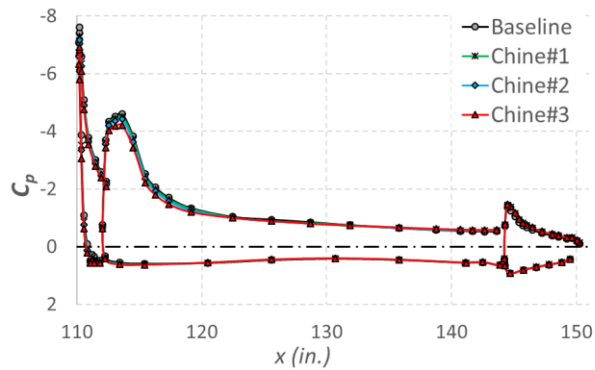
Fig. 23   Poststall ($\alpha = 18°$) C_p distributions for different chine configurations ($y = 27.8$ in.).
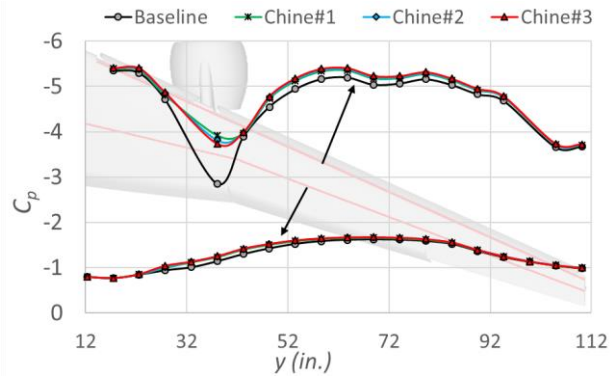
Fig. 24   Spanwise C_p distributions for different chine configurations ($\alpha = 16°$).
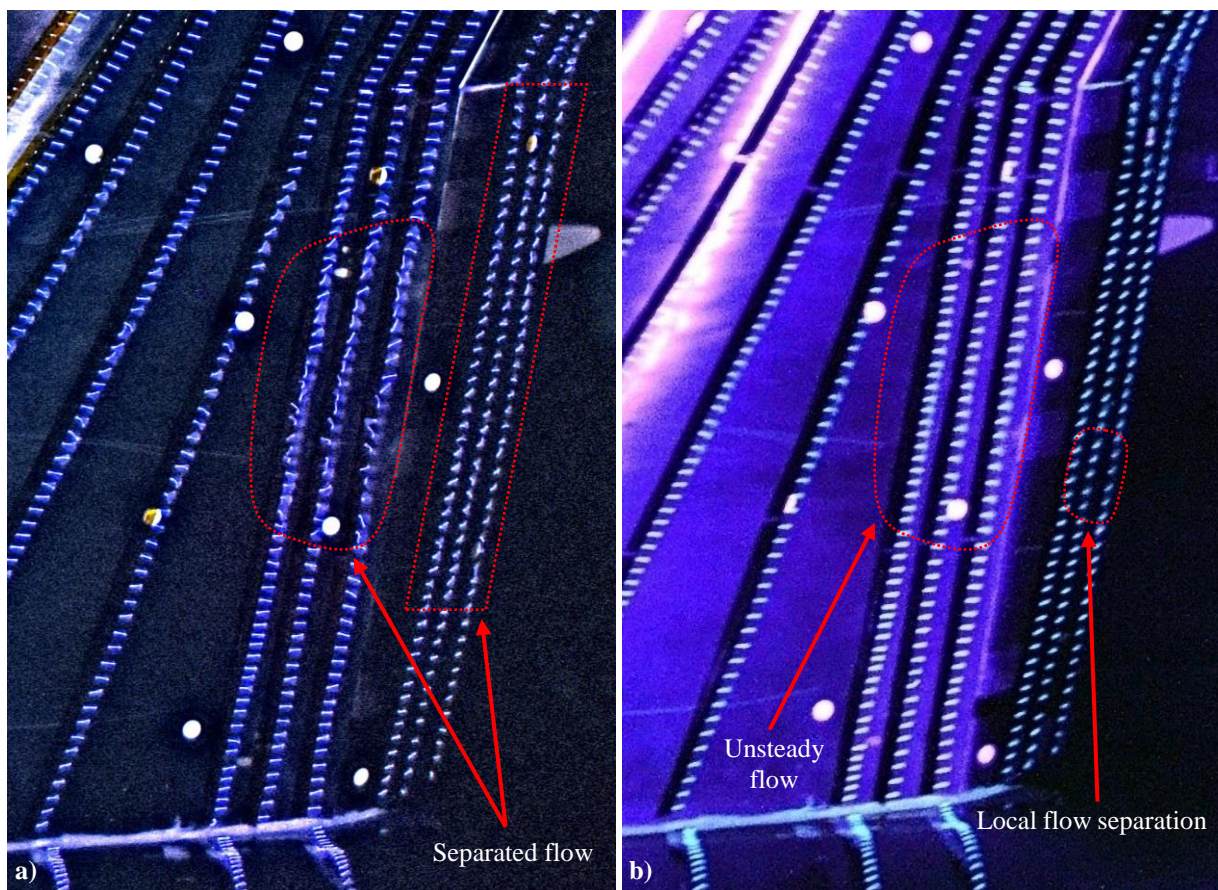
Fig. 25   Surface tuft flow visualization for the a) baseline, and b) Chine#1 configuration ($\alpha = 16°$).

24
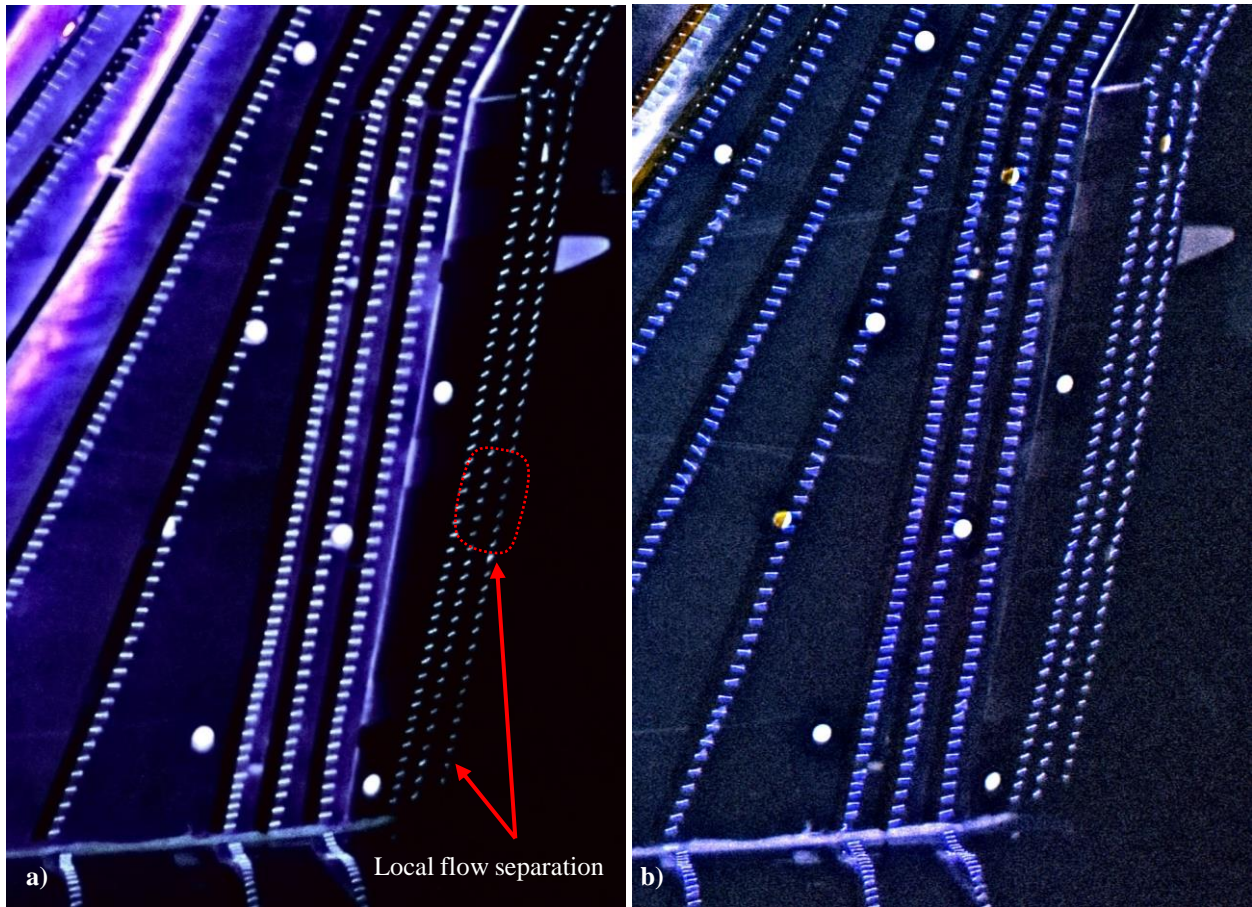
Fig. 26   Surface tuft flow visualization for the a) Chine#2, and b) Chine#3 configurations (α = 16°).
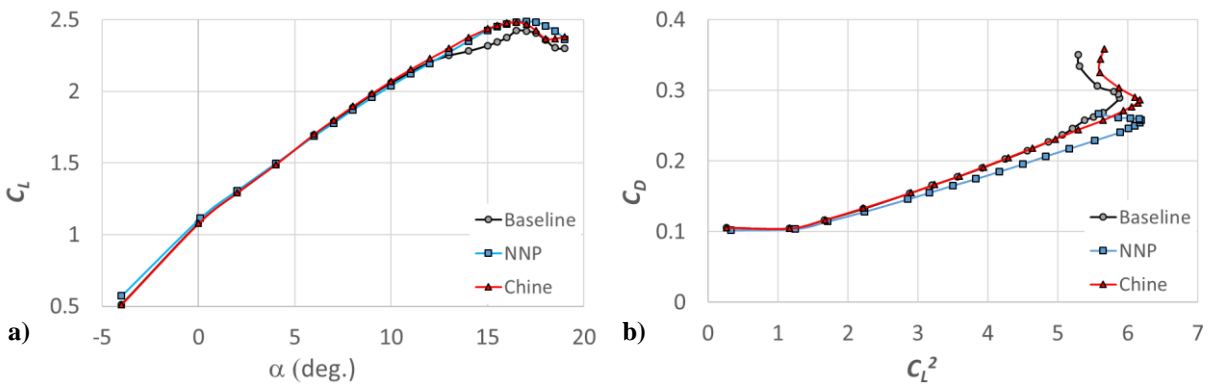
Fig. 27   Comparison of the baseline, NNP, and chine cases: a) lift curve, b) induced drag.
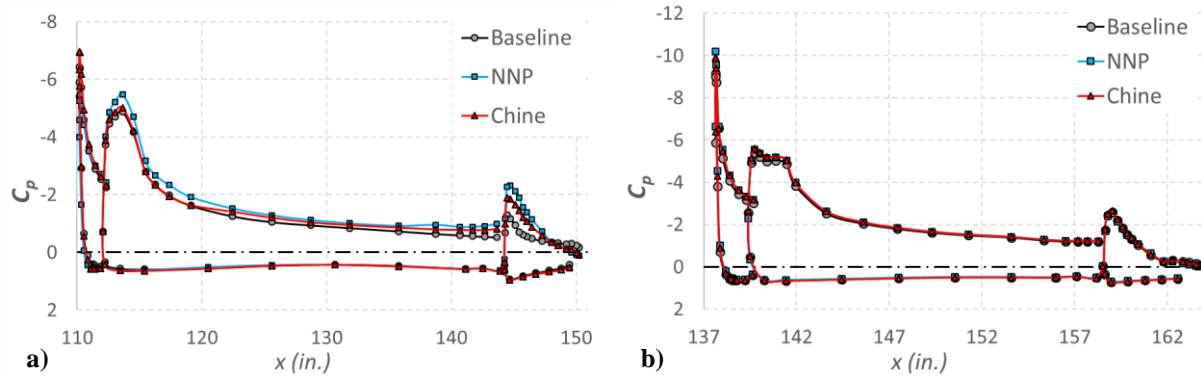
Fig. 28 C_p distributions of the baseline, NNP, and chine cases ($\alpha = 16°$): a) $y = 27.8$ in., b) $y = 63.8$ in.
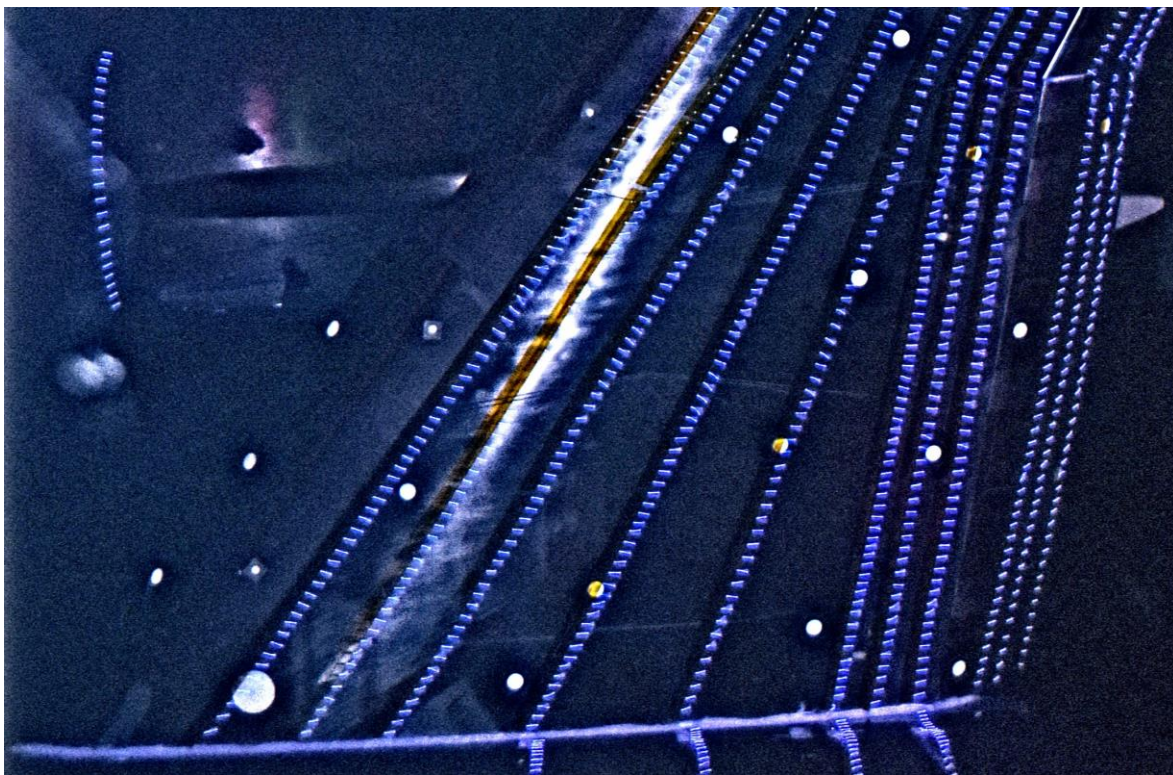
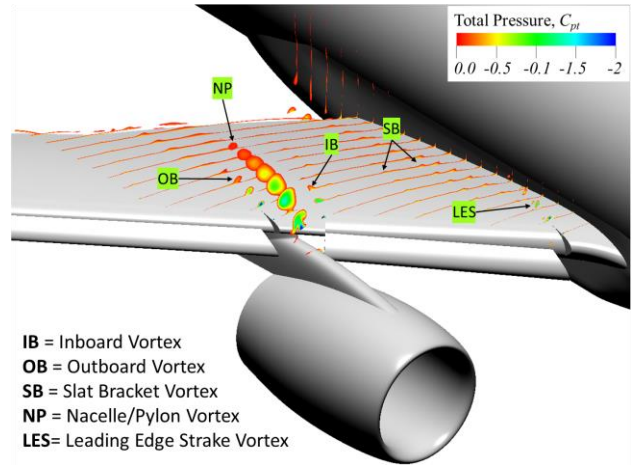**Fig. 29** Surface tuft flow visualization of the chine case at $\alpha = 16°$.

Fig. 30   Surface tuft flow visualization of the chine case at α = 18°.

IBS = Inboard Slat Vortex
OBS = Outboard Slat Vortex
IBC = Inboard Cutout Vortex
OBC = Outboard Cutout Vortex
LES = Leading Edge Strake Vortex
NP = Nacelle/Pylon Vortex
SB = Slat Bracket Vortex
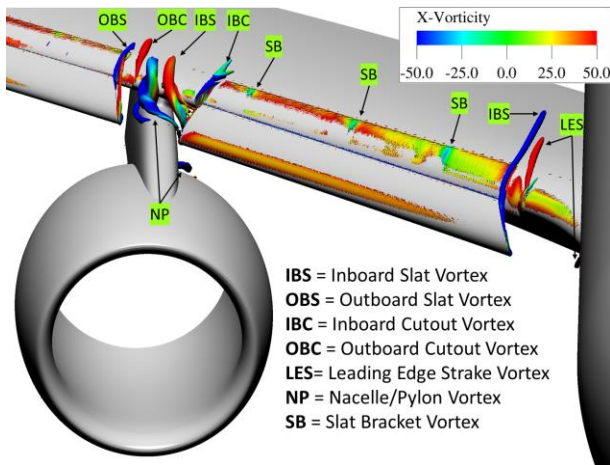
Fig. 31   Vortices generated by various parts of the CRM-HL model (α = 8°).

IB = Inboard Vortex
OB = Outboard Vortex
SB = Slat Bracket Vortex
NP = Nacelle/Pylon Vortex
LES = Leading Edge Strake Vortex

Fig. 32 C_{Pt} contours showing total pressure deficit (α = 8°).
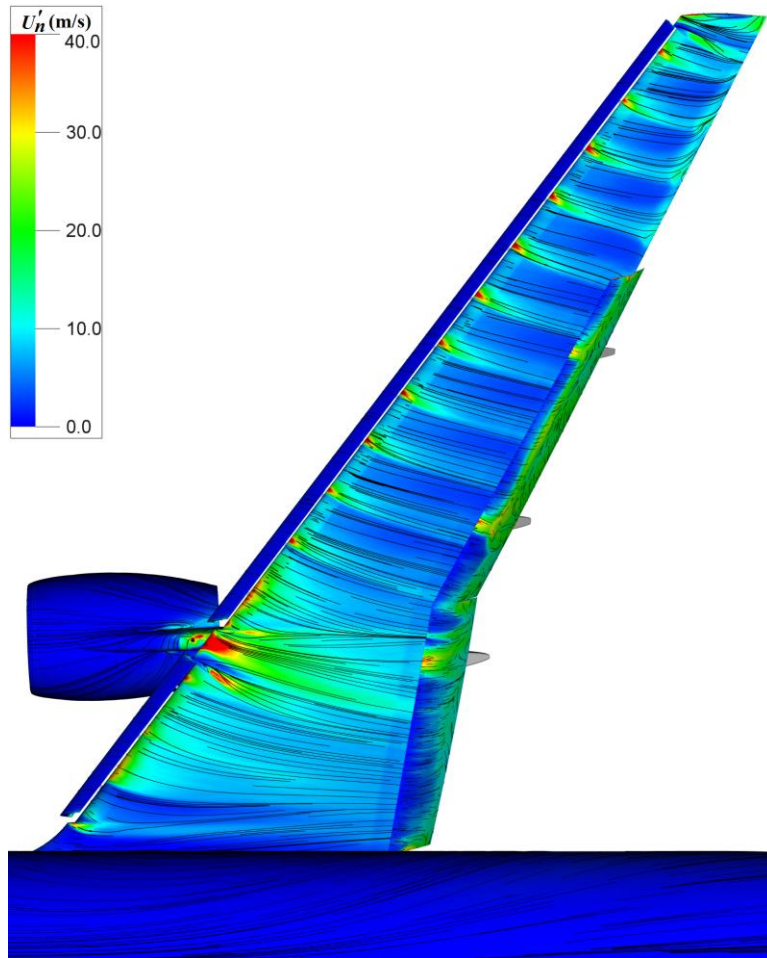
Fig. 33   Simulated surface streamlines superpositioned on velocity fluctuation contours ($\alpha = 8°$).

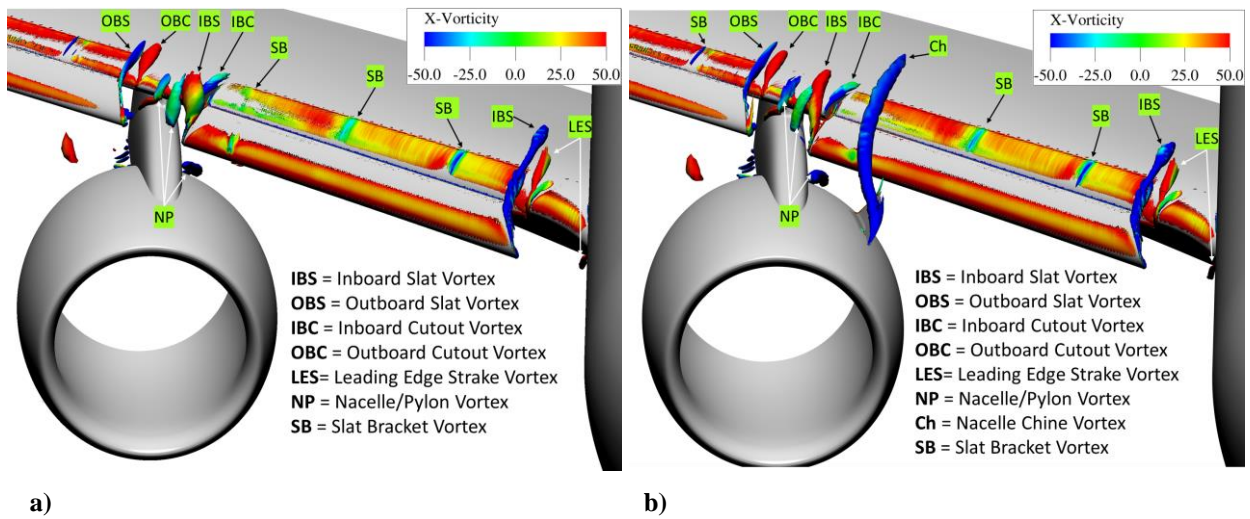a)   b)

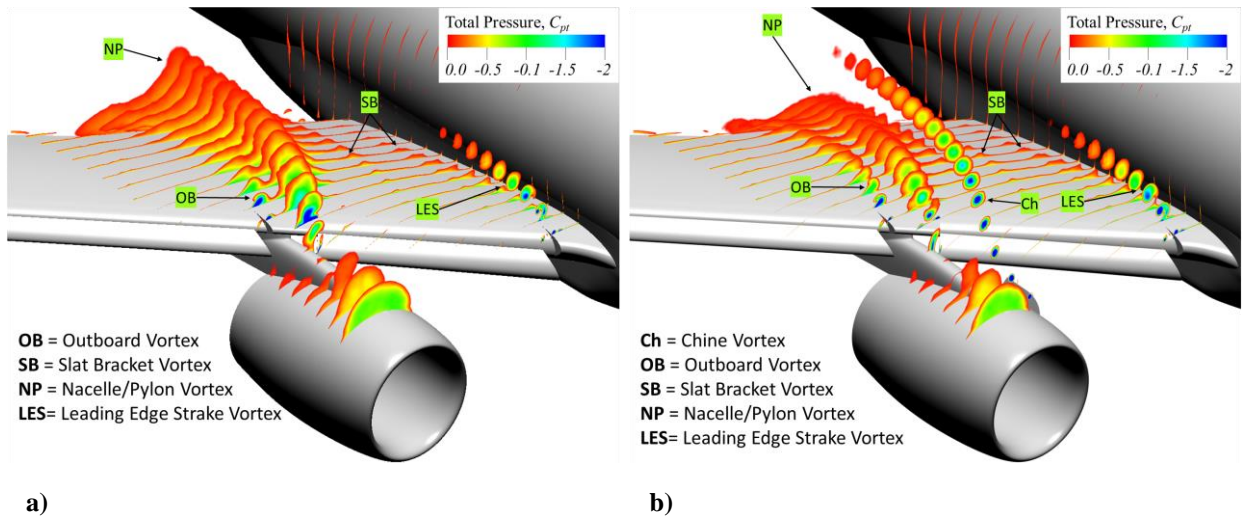**Fig. 34   Generated vortices for the a) baseline, and b) nacelle chine cases ($\alpha = 16°$).**

Fig. 35 C_{Pt} contours showing total pressure deficit for the a) baseline, and b) nacelle chine cases (α = 16°).
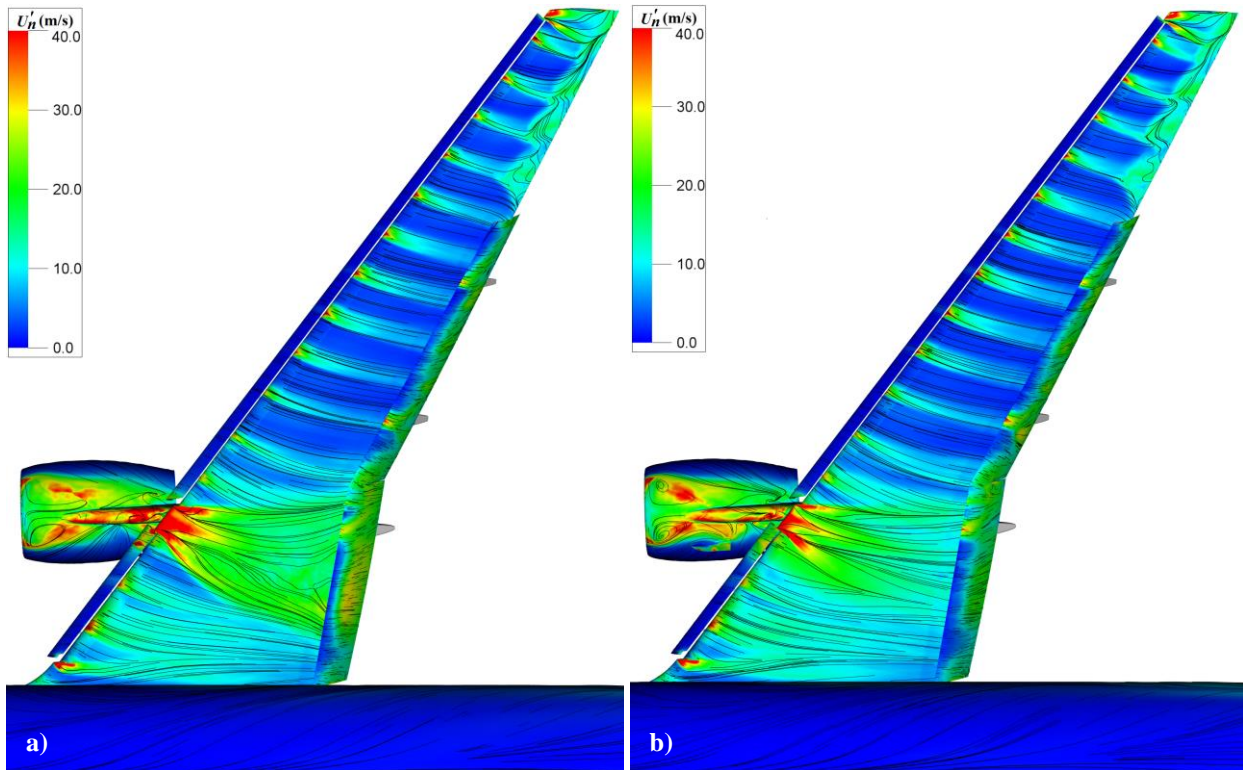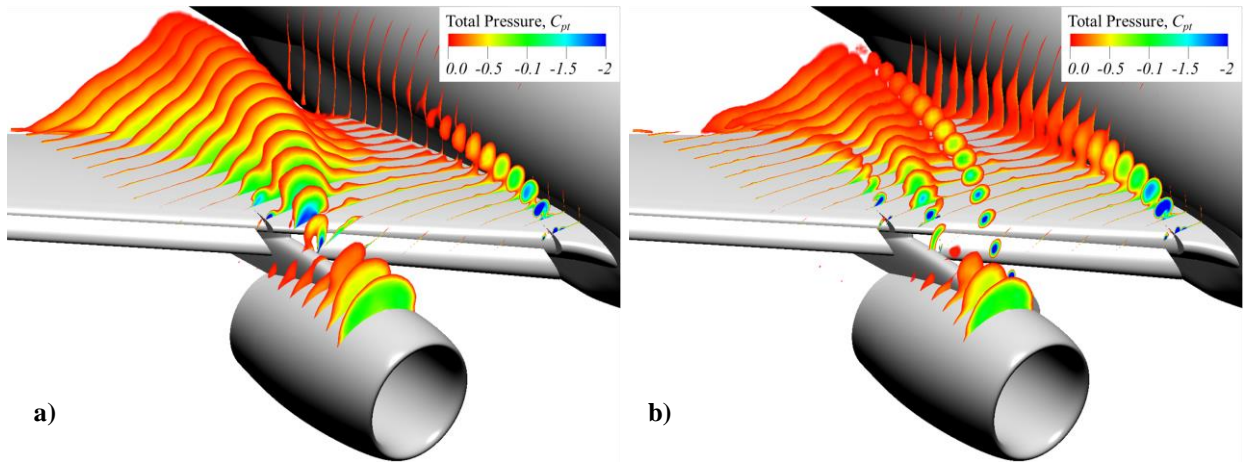

Fig. 36 Simulated surface flow visualization for the a) baseline, and b) nacelle chine cases (α = 16°).

Fig. 37 C_{Pt} contours showing total pressure deficit for the a) baseline, and b) nacelle chine cases ($\alpha = 18°$).
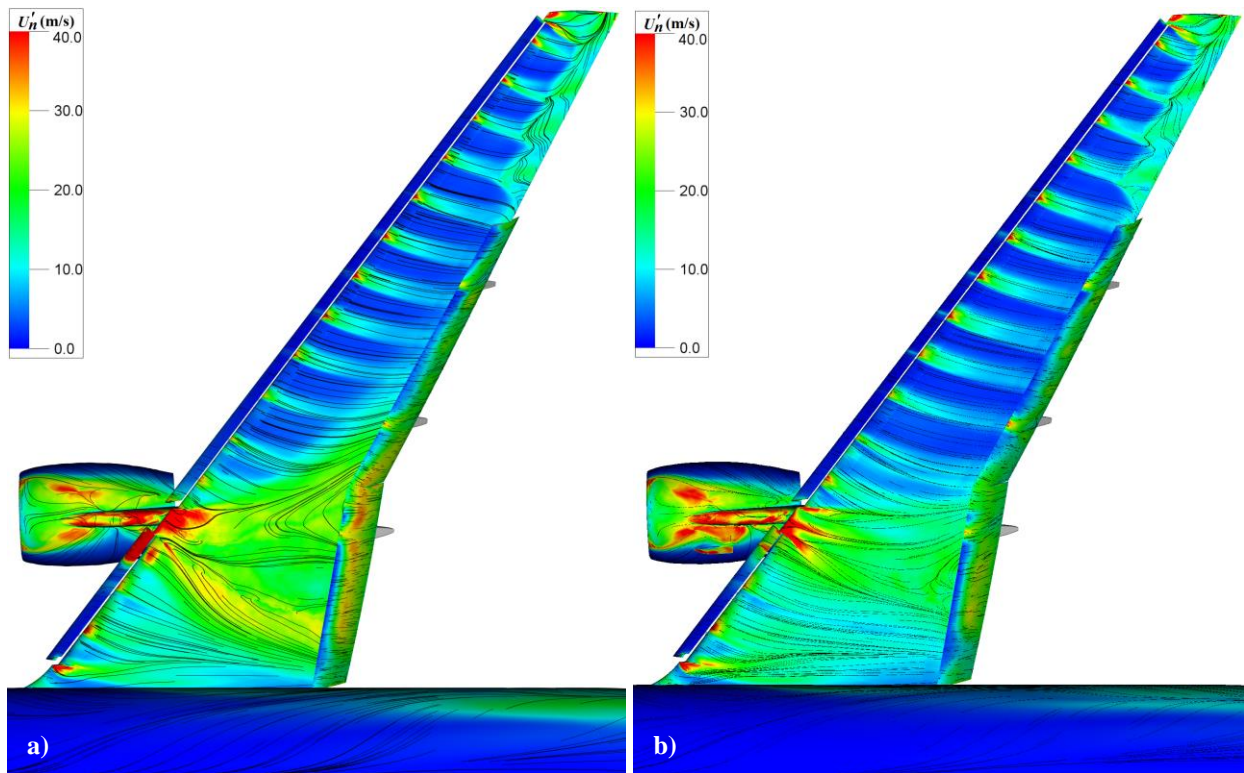

Fig. 38   Simulated surface flow visualization for the a) baseline, and b) nacelle chine cases ($\alpha = 18°$).